Rapalogs downmodulate intrinsic immunity and promote cell entry of SARS-CoV-2

Guoli Shi[1], Abhilash I. Chiramel[2], Saliha Majdoul[1], Kin Kui Lai[1], Tirhas Dempsey[1], Adam Kenney[3], Ashley Zani[3], Adrian Eddy[3], Lizhi Zhang[3], Sudipto Das[4], Paul A. Beare[5], Thorkell Andresson[4], Swagata Kar[6], Jacob S. Yount[3], Sonja M. Best[2], Alex A. Compton[1,*]

[1]HIV Dynamics and Replication Program, Center for Cancer Research, National Cancer Institute, Frederick, MD, USA

[2]Laboratory of Virology, Rocky Mountain Laboratories, National Institute of Allergy and Infectious Diseases, Hamilton, MT, USA

[3]Department of Microbial Infection and Immunity, The Ohio State University, Columbus, OH, USA

[4]Protein Characterization Laboratory, Center for Cancer Research, National Cancer Institute, Frederick, MD, USA

[5]Laboratory of Bacteriology, Rocky Mountain Laboratories, National Institute of Allergy and Infectious Diseases, Hamilton, MT, USA

[6]Bioqual, Rockville, MD, USA

[*]Address correspondence to alex.compton@nih.gov

Running title: Rapalogs promote cell entry of SARS-CoV-2

Keywords: rapamycin, rapalog, mTOR inhibitor, IFITM, interferon, SARS-CoV-2, COVID-19, coronavirus, membrane fusion, everolimus, temsirolimus, ridaforolimus, TFEB, autophagy

Abstract

SARS-CoV-2 infection in immunocompromised individuals is associated with prolonged virus shedding and the evolution of viral variants. Rapamycin and its analogs (rapalogs, including everolimus, temsirolimus, and ridaforolimus) are FDA-approved as mTOR inhibitors in clinical settings such as cancer and autoimmunity. Rapalog use is commonly associated with increased susceptibility to infection, which has been traditionally explained by impaired adaptive immunity. Here, we show that exposure to rapalogs increases susceptibility to SARS-CoV-2 infection in tissue culture and in immunologically naïve rodents by antagonizing the cell-intrinsic immune response. By identifying one rapalog (ridaforolimus) lacking this function, we demonstrate that rapalogs promote Spike-mediated entry into cells by triggering the lysosomal degradation of IFITM2 and IFITM3. Rapalogs that promote virus entry inhibit the mTOR-mediated phosphorylation of TFEB, a transcription factor controlling lysosome biogenesis and degradative capacity. In the hamster model of infection, injection of rapamycin four hours prior to virus exposure resulted in elevated virus titers in lungs and accelerated weight loss, while ridaforolimus had milder effects. Furthermore, rapamycin significantly elevated mouse-adapted SARS-CoV-2 titers in lungs of mice. Overall, our findings indicate that preexisting use of certain rapalogs may elevate host susceptibility to SARS-CoV-2 infection and disease by activating a lysosome-mediated suppression of intrinsic immunity.

Significance

Rapamycin is an immunosuppressant used in humans to treat cancer, autoimmunity, and other disease states. Here, we show that rapamycin and related compounds promote the first step of the SARS-CoV-2 infection cycle—entry into cells—by disarming cell-intrinsic immune defenses. We outline the molecular basis for this effect by identifying a rapamycin derivative that is inactive, laying the foundation for improved mTOR inhibitors that do not suppress intrinsic immunity. We find that rapamycin analogs that promote SARS-CoV-2 entry are those that activate TFEB, a transcription factor that triggers the degradation of antiviral membrane proteins inside of cells. Finally, rapamycin administration to rodents prior to SARS-CoV-2 challenge results in enhanced viral disease, revealing that its use in humans may increase susceptibility to infection.

Introduction

Severe acute respiratory syndrome (SARS) coronavirus (CoV)-2 emerged in humans in 2019 following a species jump from bats and a possible intermediate animal host and is the cause of COVID-19, a respiratory and multi-organ disease of variable severity [1, 2]. The characterization of virus-host interactions that dictate SARS-CoV-2 infection and COVID-19 severity is a major priority for public health [3]. Immune impairment, such as that resulting from cancer, has been associated with prolonged SARS-CoV-2 shedding and the seeding of "super-spreader" events [4-8].

One group of compounds being considered for the treatment of COVID-19-related immunopathology are rapamycin (sirolimus, Rapamune) and rapamycin analogs (rapalogs) [9-20]. As Food and Drug Administration-approved inhibitors of mammalian target of rapamycin (mTOR) kinase, these macrolide compounds are used therapeutically to inhibit the processes of cancer,

autoimmunity, graft versus host disease, atherosclerosis, and aging [21]. Rapalogs, including everolimus (RAD-001), temsirolimus (Torisel, CCI-779), and ridaforolimus (deforolimus, AP-23573), were developed to decrease the half-life of rapamycin *in vivo* in order to minimize the systemic immunosuppression caused by rapamycin use, which is associated with increased susceptibility to infections [22-26]. Differing by only a single functional group at carbon-40 **(Figure 1)**, it is believed that rapamycin and rapalogs share the same molecular mechanism of action to inhibit mTOR kinase—they bind to FK506-binding proteins (FKBP) and the resulting complex physically interacts with mTOR and disrupts its signaling [25, 27].

Activation of mTOR promotes cell growth, cell proliferation, and cell survival [28]. In addition, mTOR activation promotes pro-inflammatory T-cell differentiation and mTOR inhibitors have been used to block lymphocyte proliferation and cytokine storm [29]. Since respiratory virus infections like SARS-CoV-2 can cause disease by provoking hyper-inflammatory immune responses that result in immunopathology [30-32], rapalogs are being tested as treatments to decrease viral disease burden. At least three active clinical trials have been designed to test the impact of rapamycin on COVID-19 severity in infected patients (NCT04461340, NCT04341675, NCT04371640).

In addition to their potential utility for mitigating disease in individuals already infected by SARS-CoV-2, there are also calls to use rapalogs as antiviral agents to inhibit virus infection itself (i.e. as a prophylactic) [33]. It was recently shown that rapalogs inhibit SARS-CoV-2 replication when added to cells post-infection [34], attesting to a potential use of rapalogs as antivirals in infected individuals. Nonetheless, rapalogs are known to induce an immunosuppressed state in humans characterized by an increased rate of infections, including those caused by respiratory viruses. Furthermore, rapamycin administration concurrent with virus challenge has been shown to promote Influenza A replication in mice and to exacerbate viral disease [35, 36], but the mechanism was unknown. We previously found that exposure of human and murine cells to rapamycin induced the lysosomal degradation of a select group of cellular proteins, including the interferon-inducible transmembrane (IFITM) proteins, and rendered cells more permissive to infection by Influenza A virus and gene-delivering lentiviral vectors [37, 38]. IFITM1, IFITM2, and IFITM3 are expressed constitutively in a variety of tissues, are further upregulated by type-I and type-II interferons, and are important components of cell-intrinsic immunity, the antiviral network that defends individual cells against virus invasion [39, 40]. Nonetheless, it remained to be determined how rapamycin-mediated regulation of intrinsic immunity impacts host susceptibility to virus infection *in vivo*.

In this report, we show that rapalogs differentially counteract the constitutive and interferon-induced antiviral state in lung cells and increase permissiveness to SARS-CoV-2 infection. We found that the enhancing effect of rapalogs on SARS-CoV-2 infection is functionally linked to their capacity to trigger degradation of IFITM proteins, particularly IFITM2 and IFITM3. By identifying a rapalog that lacks this activity, we found that IFITM protein turnover and SARS-CoV-2 infection enhancement are associated with activation of TFEB, a master regulator of lysosome function that is regulated by mTOR. Administration of rapamycin to naive rodents four hours prior to experimental SARS-CoV-2 infection increased virus replication and viral disease severity, indicating for the first time that suppression of intrinsic immunity by rapamycin contributes to its immunosuppressive properties *in vivo*.

Results

139 **Select rapalogs promote SARS-CoV-2 infection and downmodulate IFITM proteins in lung**
140 **cells**
141
142 To assess how rapamycin and rapalogs impact SARS-CoV-2 infection, we took advantage
143 of a pseudovirus system based on human immunodeficiency virus (HIV). This pseudovirus (HIV-
144 CoV-2 S) is limited to a single round of infection, cell entry is mediated by SARS-CoV-2 Spike,
145 and infection of target cells is measured by luciferase activity. SARS-CoV-2 can enter cells via
146 multiple routes, and sequential proteolytic processing of Spike is essential to this process. SARS-
147 CoV-2 Spike is cleaved at a polybasic motif (RRAR) located at the S1/S2 boundary by furin-like
148 proteases in virus-producing cells prior to release. Subsequently, the S2' site is cleaved by the
149 trypsin-like proteases TMPRSS2 on the target cell surface or cathepsins B and L in target cell
150 endosomes, triggering membrane fusion at those sites [41-43].
151 Using A549-ACE2 (transformed human lung epithelial cells that, in addition to
152 overexpressing the ACE2 receptor, naturally express TMPRSS2), we pre-treated cells with 20 μM
153 rapamycin, everolimus, temsirolimus, ridaforolimus, or DMSO (vehicle control) for four hours
154 and then challenged cells with HIV-CoV-2. Interestingly, we found that rapalogs promoted Spike-
155 mediated infection to different extents: rapamycin, everolimus, and temsirolimus significantly
156 enhanced infection (up to 5-fold) while ridaforolimus did not **(Figure 2A)**. To determine whether
157 rapalogs promote cell permissiveness to infection by upregulating dependency factors or by
158 downregulating restriction factors, we performed the same experiment in cells pre-treated with
159 type-I interferon. While type-I interferon suppressed infection by approximately 90%, the addition
160 of rapamycin, everolimus, and temsirolimus resulted in rescue of infection by up to 20-fold
161 **(Figure 2A)**. As a result, infection levels were partially restored to those achieved in the absence
162 of interferon, with everolimus having the greatest boosting effect and ridaforolimus having no
163 effect. Therefore, rapalogs differentially promote SARS-CoV-2 Spike-mediated infection by
164 counteracting intrinsic antiviral defenses in lung cells to different extents.
165 Type-I interferon treatment of A549-ACE2 resulted in upregulation of *IFITM2* and
166 *IFITM3*, as detected by an antibody recognizing both proteins in whole cell lysates **(Figure 2B)**.
167 A549-ACE2 cells express low but detectable levels of IFITM2/3 in the absence of interferon
168 treatment **(Supplemental Figure 1A)**. Consistent with our previous publication, addition of
169 rapamycin resulted in substantial loss of IFITM2/3 protein levels from cells. In a manner that
170 mirrored the differential effects of rapalogs on pseudovirus infection, everolimus and temsirolimus
171 greatly diminished IFITM2/3 levels while ridaforolimus reduced IFITM2/3 to a lesser extent
172 **(Figure 2B)**. In contrast, ACE2 levels were not affected by interferon nor by rapalog treatment.
173 Therefore, rapamycin derivatives may facilitate infection by antagonizing constituents of intrinsic
174 immunity, including IFITM2/3, and this activity is determined by the chemical moiety found at
175 carbon-40 of the macrolide structure.
176 To extend our findings to primary lung cells, we performed similar experiments in human
177 small airway epithelial cells (HSAEC). While these cells were not permissive to HIV-CoV-2, they
178 were susceptible to infection by pseudovirus based on vesicular stomatitis virus (VSV-CoV-2)
179 whereby infection is reported by GFP expression. Pre-treatment of HSAEC with rapalogs
180 enhanced VSV-CoV-2 infection to varying extents, but as observed in A549-ACE2 cells,
181 everolimus exhibited the greatest effect and ridaforolimus, the least. Endogenous IFITM3 was
182 readily detected in HSAEC under basal conditions (in the absence of interferon), while IFITM1
183 was barely detected and IFITM2 was not detected at all, and IFITM3 levels were downmodulated
184 differentially by rapalogs **(Supplemental Figure 1B)**. siRNA-mediated knockdown of IFITM3 in

185 HSAEC resulted in enhanced VSV-CoV-2 infection, indicating that IFITM3 restricts Spike-
186 mediated infection in these cells **(Supplemental Figure 1C)**. We also treated semi-transformed
187 nasal epithelial cells known as UNCNN2TS with rapalogs in order to assess an impact on
188 endogenous IFITM3 levels. As observed in HSAEC, downmodulation of IFITM3 occurred
189 following treatment of UNCNN2TS with rapamycin, everolimus, temsirolimus, and to a lesser
190 extent, ridaforolimus **(Supplemental Figure 1D)**.
191 Since 20 μM quantities of rapalogs promoted pseudovirus infection mediated by SARS-
192 CoV-2 Spike, we tested how pretreatment of A549-ACE2 cells with varying amounts of
193 everolimus impacted infection by replication-competent SARS-CoV-2. We observed a dose-
194 dependent enhancement of infectious SARS-CoV-2 yield in supernatants of infected cells (up to
195 4-fold) **(Figure 2D)**. Therefore, everolimus boosts pseudovirus infection and SARS-CoV-2
196 infection to similar extents, and since Spike is the only viral component shared between the two
197 sources of infection, cellular entry is the infection stage inhibited by the intrinsic defenses that are
198 sensitive to downmodulation by rapalogs.
199
200 **Rapalogs facilitate cell entry mediated by various viral fusion proteins**
201
202 In order to gain a greater mechanistic understanding of the effects of rapalogs on SARS-
203 CoV-2 infection, we took advantage of HeLa cells overexpressing ACE2 (HeLa-ACE2). HeLa-
204 ACE2 were pre-treated for four hours with increasing amounts of everolimus and then challenged
205 with SARS-CoV-2. Everolimus increased titers of infectious virus released into supernatants in a
206 dose-dependent manner, and to a greater extent than was observed for A549-ACE2 cells **(Figure**
207 **3A)**. Furthermore, we found that pre-treatment of cells with 20 μM amounts of rapalogs enhanced
208 SARS-CoV-2 titers to varying extents **(Figure 3B)**. Rapamycin, everolimus, and temsirolimus
209 significantly boosted SARS-CoV-2 infection (up to 10-fold) while ridaforolimus had less of an
210 impact. We also performed infections of HeLa-ACE2 with HIV-CoV-2 pseudovirus, and the
211 results were similar—ridaforolimus was inactive while the other three compounds significantly
212 boosted Spike-mediated infection **(Figure 3C)**. To test the link between infection enhancement
213 and downmodulation of IFITM proteins by rapalogs, we probed for levels of IFITM3, IFITM2,
214 and IFITM1 by immunoblotting whole cell lysates and by immunofluorescence in intact cells using
215 specific antibodies. All IFITM proteins were readily detected in HeLa-ACE2 in the absence of
216 interferon. IFITM3, IFITM2, and IFITM1 were significantly downmodulated following treatment
217 with rapamycin, everolimus, and temsirolimus, but ridaforolimus had little to no effect on their
218 expression **(Figure 3D-E)**. In contrast, ridaforolimus reduced levels of IFITM proteins to a lesser
219 extent. Furthermore, prolonged treatment (24 hours) of cells with everolimus and temsirolimus
220 resulted in strong suppression of IFITM2 and IFITM3 protein levels **(Supplemental Figure 2A)**.
221 We confirmed that depletion of IFITM proteins by rapalogs occurs at the post-translational level,
222 since bafilomycin A1, an inhibitor of endolysosomal acidification and function, prevented their
223 loss **(Supplemental Figure 2B)**. We previously showed that lysosomal degradation of IFITM3
224 triggered by rapamycin occurs as a result of multivesicular body (MVB)-lysosome fusion, a
225 process that does not require an autophagosome intermediate [44]. Here, we used SAR405, a
226 selective inhibitor of phosphatidylinositol-3-phosphate (PI3P) production by vps34/PI3KC3 [45]
227 to prevent macroautophagy induction. At a concentration sufficient to reduce intracellular PI3P
228 **(Supplemental Figure 2C)**, SAR405 did not prevent degradation of IFITM2/3 following
229 treatment with rapamycin, everolimus, or temsirolimus **(Supplemental Figure 2D)**. Therefore,
230 rapamycin and specific rapalogs trigger the degradation of endogenous factors mediating intrinsic

231 resistance to SARS-CoV-2 infection, including the IFITM proteins, by promoting their turnover
232 in lysosomes via the macroautophagy-independent MVB pathway.
233 Enveloped virus entry into cells is a concerted process involving virus attachment to the
234 cell surface followed by fusion of cellular and viral membranes. Since IFITM proteins are known
235 to inhibit virus-cell membrane fusion, we quantified the terminal stage of HIV-CoV-2 entry by
236 tracking the cytosolic delivery of beta-lactamase (BlaM) in single cells. We found that treatment
237 of cells with rapamycin, everolimus, and temsirolimus resulted in enhanced HIV-CoV-2 entry
238 while ridaforolimus had no such effect **(Figure 4A)**. To measure whether rapalogs promote the
239 cell entry process driven by other coronavirus Spike proteins, we produced HIV incorporating
240 Spike from SARS-CoV (HIV-CoV-1) or MERS-CoV (HIV-MERS-CoV). Infections by both HIV-
241 CoV-1 and HIV-MERS-CoV were elevated by rapalog treatment in HeLa-ACE2 and HeLa-DPP4,
242 respectively, although the extent of enhancement was lower than that observed with HIV-CoV-2
243 **(Figure 4B-C)**. Consistently, ridaforolimus was the least active among the rapalogs tested and it
244 did not significantly promote pseudovirus infection. Since we previously showed that rapamycin
245 promoted the cellular entry of Influenza A virus and VSV-G pseudotyped lentiviral vectors [44],
246 we also assessed infection of pseudoviruses incorporating hemagglutinin (HIV-HA) or VSV G
247 (HIV-VSV G). Rapamycin, everolimus, and especially temsirolimus boosted HA- and VSV G-
248 mediated infections (up to 30-fold and 11-fold, respectively), while ridaforolimus was inactive
249 **(Figure 4D-E)**. Since IFITM proteins have been previously shown to inhibit infection by SARS-
250 CoV-1, MERS-CoV, VSV, and Influenza A virus [40], these data suggest that rapalogs promote
251 infection, at least in part, by lowering the barrier to virus entry imposed by IFITM proteins.
252
253 **IFITM2/3 mediate the rapalog-sensitive barrier to SARS-CoV-2 infection in HeLa-ACE2**
254
255 To formally address how rapalog-mediated depletion of IFITM proteins impacts SARS-
256 CoV-2 Spike-mediated entry, we used HeLa cells in which IFITM1, IFITM2, and IFITM3 are
257 knocked out (*IFITM1-3* KO) and introduced human ACE2 by transient transfection
258 **(Supplemental Figure 3A)**. IFITM2 alone or both IFITM2 and IFITM3 were restored in *IFITM1-*
259 *3* KO cells by transient overexpression **(Supplemental Figure 3B)** and cells were challenged with
260 HIV-CoV-2. Relative to WT cells, HIV-CoV-2 infection was approximately 50-fold higher in
261 *IFITM1-3* KO cells, indicating that endogenous IFITM proteins restrict SARS-CoV-2 Spike-
262 mediated infection. Furthermore, while temsirolimus significantly promoted infection by 10-fold
263 in WT cells, little to no enhancement was observed in *IFITM1-3* KO cells **(Supplemental Figure**
264 **3C)**. Ectopic expression of IFITM2 inhibited infection and partially restored sensitivity to
265 temsirolimus, while the combination of IFITM2 and IFITM3 restricted infection further and fully
266 restored temsirolimus sensitivity. These findings indicate that temsirolimus promotes Spike-
267 mediated infection in HeLa-ACE2 cells by lowering levels of endogenous IFITM2 and IFITM3.
268
269 **Rapalogs differentially activate a lysosomal degradation pathway orchestrated by TFEB**
270
271 Since rapamycin and rapalogs are known to inhibit signaling by mTOR by binding both
272 mTOR and FKBP12 (and other FKBP members), we sought to determine whether mTOR binding
273 and its inhibition are required for rapalog-mediated enhancement of SARS-CoV-2 infection. To
274 that end, we tested the effect of tacrolimus (also known as FK506), a macrolide
275 immunosuppressant that is chemically related to rapalogs but does not bind nor inhibit mTOR.
276 Instead, tacrolimus forms a ternary complex with FKBP12 and calcineurin to inhibit the signaling

277 properties of the latter [46]. In HeLa-ACE2 cells, a four-hour treatment of 20 μM tacrolimus did
278 not reduce levels of IFITM2/3 **(Supplemental Figure 4A)**, nor did it boost HIV-CoV-2 infection
279 **(Supplemental Figure 4B)**. These results suggest that FKBP12 binding is not sufficient for drug-
280 mediated enhancement of SARS-CoV-2 infection. They also suggest that the extent to which
281 mTOR is inhibited may explain the differential degree to which infection is impacted by the
282 immunosuppressants examined in this study. Therefore, we surveyed the phosphorylation status
283 of TFEB, a transcription factor that controls lysosome biogenesis and degradative processes
284 carried out by lysosomes [47]. mTOR phosphorylates TFEB at serine 211 (S211), which promotes
285 its sequestration in the cell cytoplasm and decreases its translocation into the nucleus [47-49].
286 Furthermore, this phosphorylation event was previously shown to be sensitive to inhibition by
287 rapamycin and temsirolimus [48, 50]. We found that rapamycin, everolimus, and temsirolimus
288 significantly reduced S211 phosphorylation of endogenous TFEB in A549-ACE2 cells while
289 ridaforolimus did not **(Figure 5A-B)**. Loss of pTFEB (S211) following treatment with
290 temsirolimus was associated with significantly elevated protein levels of several TFEB-regulated
291 genes (cathepsin L, VAMP8, syntaxin 8, M6PR, and SCAMP2 [51, 52]) as measured using
292 proteomics by mass spectrometry **(Figure 5C)**.
293 We also assessed the effect of temsirolimus and ridaforolimus on TFEB phosphorylation
294 in HeLa-ACE2 cells. As observed in A549-ACE2, temsirolimus significantly reduced pTFEB
295 (S211) levels while ridaforolimus did not **(Figure 6A-B**). Furthermore, we measured the
296 subcellular distribution of TFEB-GFP in HeLa-ACE2 treated with different compounds and found
297 that, compared to ridaforolimus, temsirolimus induced a significantly greater accumulation of
298 TFEB-GFP in the nucleus **(Figure 6C-D)**. These findings suggest that ridaforolimus exhibits a
299 less potent inhibition of mTOR-mediated TFEB phosphorylation. Therefore, nuclear translocation
300 of TFEB is associated with IFITM2/3 degradation and increased cellular susceptibility to SARS-
301 CoV-2 Spike-mediated infection. Consistent with a direct relationship between TFEB activation,
302 IFITM2/3 turnover, and Spike-mediated cell entry, we found that ectopic expression of a
303 constitutively active form of TFEB lacking the first 30 amino-terminal residues [47] was sufficient
304 to trigger IFITM2/3 loss from cells **(Figure 6F-G)** and sufficient to increase susceptibility to HIV-
305 CoV-2 infection **(Figure 6H)**. In summary, our results employing functionally divergent rapalogs
306 reveal a previously unrecognized immunoregulatory role played by the mTOR-TFEB-lysosome
307 axis that affects the cell entry of SARS-CoV-2 and other viruses.
308
309 **Rapamycin enhances SARS-CoV-2 infection and viral disease *in vivo***
310
311 Our findings from SARS-CoV-2 and pseudovirus infection of human cells demonstrate
312 that rapamycin, everolimus, and temsirolimus can suppress intrinsic immunity at the post-
313 translational level, while ridaforolimus does not. However, whether these compounds are
314 functionally divergent when administered *in vivo* was unclear. Since temsirolimus is a prodrug of
315 rapamycin (it is metabolized to rapamycin), and since rapamycin was previously shown to promote
316 morbidity of Influenza A infection in mice [36, 53], we tested how intraperitoneal injection of
317 rapamycin, ridaforolimus, or DMSO before intranasal challenge with SARS-CoV-2 impacted
318 virus replication and disease course in naïve hamsters **(Figure 7A)**. Hamsters are a permissive
319 model for SARS-CoV-2 because hamster ACE2 is sufficiently similar to human ACE2 to support
320 productive infection. Furthermore, in contrast to transgenic mice expressing human ACE2 or mice
321 infected with mouse-adapted (MA) SARS-CoV-2, hamsters exhibit severe disease characterized
322 by lung pathology when high viral loads are achieved [54]. Four hamsters were randomly allocated

323 to each group. Relative to DMSO treatment, hamsters injected with rapamycin four hours prior to
324 challenge exhibited a significantly greater loss of body weight at days 2-5 post-infection **(Figure**
325 **7B)**. In contrast, ridaforolimus treatment impacted weight loss to a slightly lesser extent, with
326 significant differences from DMSO apparent at days 3 and 4 post-infection. While none of the
327 hamsters treated with DMSO exhibited severe weight loss necessitating euthanasia and body
328 weights recovered, three of the four animals treated with rapamycin were euthanized on day 7
329 post-infection, and the fourth animal was found dead on day 8. Meanwhile, two of the four
330 hamsters treated with ridaforolimus met requirements for euthanasia on day 7 post-infection, and
331 the two survivors recovered body weight between days 8 and 10 post-infection **(Figure 7B)**. As a
332 result, hamsters treated with rapamycin exhibited significantly reduced survival compared to the
333 DMSO group **(Figure 7C)**. Early SARS-CoV-2 replication was measured by quantitative PCR
334 from oral swabs taken on day 2 post-infection. While there was large variance among hamsters in
335 the DMSO group, rapamycin-treated hamsters exhibited a higher viral burden on average while
336 ridaforolimus-treated hamsters exhibited more moderate increases **(Figure 7D)**. Terminal viral
337 titers in lungs were also measured following euthanasia. Infectious virus was undetectable in the
338 lungs of DMSO-treated hamsters on day 10 post-infection, indicative of viral clearance **(Figure**
339 **7E)**. In contrast, infectious virus was detected in lungs of the three rapamycin-treated hamsters
340 that were euthanized on day 7 post-infection (the fourth hamster that was found dead on day 8 was
341 not examined). By comparison, virus detected in lungs of two ridaforolimus-treated hamsters
342 euthanized on the same day were lower on average. No infectious virus was detected in lungs from
343 the remaining two hamsters treated with ridaforolimus that survived until the end of the study.
344 Overall, these results suggest that rapamycin administration just prior to SARS-CoV-2 exposure
345 increases host susceptibility to infection and significantly increases morbidity and mortality in a
346 manner that is associated with elevated virus replication.
347 We previously found that, like its human counterpart, murine IFITM3 is sensitive to
348 depletion by rapamycin [44]. To confirm that rapamycin promotes host susceptibility to SARS-
349 CoV-2 infection, we injected C57BL/6 mice with rapamycin or DMSO four hours prior to
350 challenge with MA SARS-CoV-2 and measured infectious viral burden in lungs upon euthanasia
351 on day 2 post-infection **(Figure 7F)**. We found that virus titers were significantly increased (144-
352 fold) in rapamycin-treated mice compared to DMSO-treated mice **(Figure 7G)**, supporting the
353 notion that rapamycin downmodulates intrinsic barriers to infection *in vivo*.
354
355 **Discussion**
356
357 By assessing their impact on infection at the single-cell and whole-organism level, we draw
358 attention to an immunosuppressive property of rapamycin and some rapalogs that acts on cell-
359 intrinsic immunity and increases cellular susceptibility to infection by SARS-CoV-2 and likely
360 other pathogenic viruses. Side effects of rapalog use in humans, including increased risk of
361 respiratory tract infections, are regularly attributed to immunosuppression of adaptive immunity
362 [55]. Indeed, rapalogs have been used to mitigate systemic immunopathology caused by T-cell
363 responses, and this is one reason why they are being tested for therapeutic benefit in COVID-19
364 patients. However, by injecting rapamycin into immunologically naïve hosts just prior to virus
365 challenge, it is unlikely that rapalogs used in our experiments modulated adaptive immunity
366 against SARS-CoV-2. Therefore, while immunomodulation of adaptive immunity by rapalogs
367 may provide benefit for patients already suffering from COVID-19, pre-existing rapalog use may
368 enhance susceptibility by counteracting cell-intrinsic immunity. The injection dose of rapamycin

369 or ridaforolimus (3 mg/kg) that we administered once to hamsters or daily to mice, when adjusted
370 for body surface area and an average human weight of 60 kg [56], equates to approximately 15 mg
371 per human. This figure is similar to those administered to humans in clinical settings, such as the
372 use of rapamycin for the treatment of glioblastoma (up to 10 mg daily for multiple days) or the use
373 of temsirolimus for the treatment of renal cell carcinoma (25 mg once weekly) [23, 57, 58].
374 Therefore, our results may provide new insight into how rapamycin and rapalogs elicit unintended
375 immunocompromised states in humans.
376 By leveraging the differential functional properties of rapalogs, we reveal how the mTOR-
377 TFEB-lysosome axis impacts intrinsic resistance to SARS-CoV-2 and other virus infections.
378 Specifically, rapamycin and select rapalogs (everolimus and temsirolimus) promote infection at
379 the stage of cell entry, and this is functionally associated with nuclear accumulation of TFEB and
380 the lysosomal degradation of IFITM proteins **(Figure 8)**. While mTOR phosphorylates TFEB at
381 S211 to promote the sequestration of TFEB in the cytoplasm, the phosphatase calcineurin
382 dephosphorylates TFEB at this position to promote nuclear translocation [59]. Therefore, the
383 extent to which different rapalogs promote nuclear TFEB accumulation may be a consequence of
384 differential mTOR inhibition and/or differential calcineurin activation. Calcineurin is activated by
385 calcium release through the lysosomal calcium channel TRPML1 (also known as mucolipin-1)
386 [59], and interestingly, it was shown that rapamycin and temsirolimus, but not ridaforolimus,
387 promote calcium release by TRPML1 [50]. Therefore, it is worth examining whether TRPML1 or
388 related lysosomal calcium channels are required for the effects of rapalogs on virus infection.
389 Overall, our findings reveal a previously unrecognized mechanism by which TFEB promotes virus
390 infections—inhibition of cell-intrinsic defenses restricting virus entry. We show that nuclear TFEB
391 induces the degradation of IFITM proteins, but it may also trigger the loss or relocalization of other
392 antiviral factors. Furthermore, TFEB-mediated induction of dependency factors, such as cathepsin
393 L, is likely to partially contribute to the overall impact of rapalogs on SARS-CoV-2 infection. Our
394 proteomics dataset will facilitate the identification of additional factors regulated by
395 rapalogs/TFEB that play positive and negative roles during SARS-CoV-2 and other virus
396 infections. Nonetheless, this work identifies TFEB as a therapeutic target, and inhibitors that limit
397 levels of nuclear TFEB could be mobilized for broad-spectrum antiviral activity.
398 We previously demonstrated that treatment of cells with micromolar quantities of
399 rapamycin induced the lysosomal degradation of IFITM2/3 via a pathway that is independent of
400 macroautophagy yet dependent upon endosomal complexes required for transport (ESCRT)-
401 mediated sorting of IFITM2/3 into intraluminal vesicles of late endosomes/MVB [37]. This MVB-
402 mediated degradation pathway is also referred to as microautophagy, which occurs directly on
403 endosomal or lysosomal membranes and involves membrane invagination [60]. In both yeast and
404 mammalian cells, microautophagy is characterized by ESCRT-dependent sorting of
405 endolysosomal membrane proteins into intraluminal vesicles followed by their degradation by
406 lysosomal hydrolases [61]. While microautophagy selectively targets ubiquitinated endolysosomal
407 membrane proteins, cytosolic proteins can also be non-selectively internalized into intraluminal
408 vesicles and degraded [62, 63]. Interestingly, microautophagy is known to be regulated by mTOR
409 [64, 65], and mTOR inhibition triggers a ubiquitin- and ESCRT-dependent turnover of vacuolar
410 (lysosomal) membrane proteins in yeast [66, 67]. Overall, our findings suggest that select rapalogs
411 induce a rapid endolysosomal membrane remodeling program controlled by TFEB, and IFITM
412 proteins are among the client proteins subjected to this pathway. The full cast of cellular factors
413 that orchestrate this selective degradation program in mammalian cells and the other client proteins
414 subjected to it will need to be worked out. Interestingly, the E3 ubiquitin ligase NEDD4 was

415 previously shown to ubiquitinate IFITM2 and IFITM3 and to induce their lysosomal degradation
416 in mammalian cells [68, 69], while Rsp5, the yeast ortholog of NEDD4, was shown to ubiquitinate
417 vacuolar proteins turned over by microautophagy in yeast [70]. Therefore, rapamycin and select
418 rapalogs may upregulate NEDD4 function, resulting in selective degradation of a subset of the
419 cellular proteome that includes IFITM proteins. Indeed, NEDD4 and the related NEDD4L are
420 among the known target genes regulated by TFEB [52].
421 The relationship between IFITM proteins and human coronaviruses is complex. It was
422 previously shown that IFITM3 facilitates replication of the seasonal coronavirus hCoV-OC43 [71],
423 while we and others recently showed that SARS-CoV-1 and SARS-CoV-2 infection is inhibited
424 by ectopic and endogenous IFITM1, IFITM2, and IFITM3 from mice and humans [72-76].
425 Intriguingly, mutants of human IFITM3 that lack the capacity to internalize into endosomes lost
426 antiviral activity and promoted SARS-CoV-2 and MERS-CoV infection, revealing that IFITM3
427 can either inhibit or enhance infection depending on its subcellular localization [72, 77].
428 Furthermore, one study reported that endogenous human IFITM proteins promoted infection by
429 SARS-CoV-2 in certain human tissues [78]. Overall, the net effect of human IFITM proteins on
430 SARS-CoV-2 infection *in vivo* remains unclear. However, the impact of rapamycin in our
431 experimental SARS-CoV-2 infections of hamsters and mice suggests that rapamycin-mediated
432 loss of IFITM proteins favors virus infection and viral disease, consistent with IFITM proteins
433 performing antiviral roles against SARS-CoV-2 in those species.
434 Other lines of evidence support an antiviral role for IFITM proteins during SARS-CoV-2
435 infection in humans. While SARS-CoV-2 infection has been shown to cause deficiencies in
436 interferon synthesis and interferon response pathways, administration of type I interferon *in vivo*
437 promotes SARS-CoV-2 clearance in hamsters and humans [79]. Notably, IFITM3 is among the
438 most highly induced genes in primary human lung epithelial cells exposed to SARS-CoV-2 [80,
439 81], and humans experiencing mild or moderative COVID-19 showed elevated induction of
440 antiviral genes, including *IFITM1* and *IFITM3*, in airway epithelium compared to individuals
441 suffering from more severe COVID-19 [82]. Single nucleotide polymorphisms in human *IFITM3*
442 known as ns12252 and rs34481144, which lead to IFITM3 loss-of-function, have been associated
443 with severe outcomes following Influenza A virus infection as well as severe COVID-19 [83, 84].
444 These data suggest that cell-intrinsic immunity in airways plays a role in restricting virus spread
445 and constraining systemic pathology during infection. Therefore, downmodulation of IFITM
446 proteins, and possibly other cellular proteins, by select rapalogs may contribute to the
447 immunocompromised state that these drugs are well known to elicit in humans. This possibility
448 warrants the close examination of different rapalog regimens on respiratory virus acquisition and
449 disease in humans.
450
451 **Materials and Methods**
452
453 **Cell lines, cell culture, inhibitors, and cytokines**
454
455 HEK293T cells were obtained from ATCC (CRL-3216). HeLa-ACE2, HeLa-DPP4, and A549-
456 ACE2 cell lines were produced by transducing cells with lentivirus packaging pWPI encoding
457 ACE2 or DPP4 and selecting with blasticidin. HeLa IFITM1/2/3 Knockout (C5-9) cells were
458 purchased from ATCC (CRL-3452). Primary human small airway (lung) epithelial cells (HSAEC)
459 were purchased from ATCC (PCS-301-010). The partially immortalized nasal epithelial cell line
460 (UNCNN2TS) was kindly provided by Scott H. Randell (University of North Carolina School of

461 Medicine). Vero E6 cells (NR-53726) were obtained from BEI Resources. Vero-TMPRSS2 cells
462 were a kind gift from Shan-Lu Liu (The Ohio State University). All cells were cultured at 37°C
463 with 5% CO_2 in Dulbecco's Modified Eagle Medium (DMEM) supplemented with 10% fetal
464 bovine serum (HyClone, Cytiva), except for UNCNN2TS, which were cultured in EpiX Medium
465 (Propagenix), and HSAEC, which were cultured with airway epithelial cell basal medium (ATCC,
466 PCS-300-030) and the bronchial epithelial cell growth kit (ATCC, PCS-300-040). Rapamycin
467 (553211) was obtained from Sigma. Everolimus (S1120), temsirolimus (S1044), ridaforolimus
468 (S5003), tacrolimus (S5003), and SAR405 (S7682) were obtained from Selleckchem. Type-I
469 interferon (human recombinant interferon-beta$_{ser17}$, NR-3085) was obtained from BEI Resources.
470
471 **Plasmids and RNA interference**
472
473 pcDNA3.1 encoding human ACE2 was kindly provided by Thomas Gallagher (Loyola
474 University). pcDNA3.1 encoding CoV-1 Spike or CoV-2 Spike tagged with a C9 epitope on the
475 C-terminus, or MERS Spike, was kindly provided by Thomas Gallagher (Loyola University).
476 pcDNA3.1 encoding CoV-1 Spike or CoV-2 Spike tagged with a FLAG epitope on the C-terminus
477 was obtained from Michael Letko and Vincent Munster (NIAID). pMD2.G encoding VSV-G
478 (12259) was obtained from Addgene (a generous gift from Didier Trono). pWPI was obtained
479 from Addgene (12254) and human ACE2 or human TMPRSS2 was introduced by Gateway
480 cloning (Gateway LR Clonase II Enzyme mix (11791020)) as per manufacturer's instructions.
481 pPolII encoding hemagglutinin (HA) or neuraminidase (NA) from Influenza A/Turkey/1/2005
482 (H5N1) were kindly provided by Richard Yi Tsun Kao (The University of Hong Kong). pCMV
483 encoding HIV-1 Vpr fused to beta lactamase (pCMV4-BlaM-Vpr) was obtained from Addgene
484 (21950). A plasmid encoding replication-incompetent HIV-1 lacking *env* and *vpr* and encoding
485 luciferase (pNL4-3LucR-E-) was kindly provided by Vineet KewalRamani (National Cancer
486 Institute). A plasmid encoding replication-incompetent HIV-1 lacking *env* (pNL4-3E-) was kindly
487 provided by Olivier Schwartz (Institut Pasteur). pEGFP-N1-TFEB (38119) and pEGF-N1-
488 Δ30TFEB (44445) were obtained from Addgene (a generous gift of Shawn M. Ferguson). pEGFP-
489 2xFYVE (140047) was obtained from Addgene (a gift from Harald Stenmark). Silencer Select
490 siRNA targeting IFITM3 (s195035) and a non-targeting control (No. 1) was obtained from
491 Ambion. Cells were transfected with 20 nM siRNA using Opti-MEM (Gibco) and Lipofectamine
492 RNAiMAX (Thermo Fisher).
493
494 **Virus and pseudovirus infections**
495
496 SARS-CoV-2 isolate USA-WA1/2020 (MN985325.1) was provided by the Centers for Disease
497 Control or by BEI Resources (NR-52281). Virus propagation was performed in Vero E6 cells.
498 Mouse-adapted (MA) SARS-CoV-2 variant MA10 (in the USA-WA1/2020 backbone) [85] was
499 obtained from BEI Resources (NR-55329). Virus propagation was performed in Vero E6 cells and
500 subsequently in Vero-TMPRSS2 cells. Virus was sequenced to ensure lack of tissue culture
501 adaptations, including furin cleavage site mutations. Virus titers were calculated by plaque assay
502 performed in Vero E6 cells as follows: serial 10-fold dilutions were added to Vero E6 monolayers
503 in 48-well plates for 1 hour at 37°C. Cells were overlayed with 1.5% carboxymethyl cellulose
504 (Sigma) in modified Eagle's medium containing 3% fetal bovine serum (Gibco), 1 mM L-
505 glutamine, 50 units per mL penicillin and 50 µg per mL streptomycin. Three days post-infection,
506 cells were fixed in 10% formalin and stained with crystal violet to visualize and count plaques as

507 previously described [86]. Titers were calculated as plaque forming units per mL and normalized
508 as described in the figure captions. HIV-based pseudovirus was produced by transfecting
509 HEK293T cells with 12 µg of pNL4-3LucR-E- and 4 µg of plasmid encoding viral glycoproteins
510 (pcDNA3.1 Spike (CoV-1, CoV-2, or MERS), pMD2.G-VSV-G, or 2 µg of pPol1II-HA and 2 µg
511 of pPol1II-NA) using TransIT-293 (Mirus). Virus supernatant was harvested 72 hours post-
512 transfection and filtered through 0.22 µm filters. Pseudovirus titers were determined by p24 ELISA
513 (XpressBio) and 100 ng p24 equivalent was added to target cells and incubated for 72 hours prior
514 to lysis with Passive Lysis Buffer (Promega). Luciferase activity was measured using the
515 Luciferase Assay System (Promega). VSV-based pseudovirus was produced as previously
516 described [87]. In brief, HEK293T cells were transfected with 2 µg pcDNA3.1 CoV-1, CoV-2, or
517 MERS Spike using Lipofectamine2000 (Thermo Fisher). At 24 hours post-transfection, culture
518 medium was removed from cells and 2 mL of VSV-luc/GFP + VSV-G (seed particles) was added.
519 At 48 hours post-infection, virus supernatants were collected, clarified by centrifugation at 500xG
520 for 5 mins, and stored. 50 µL of virus supernatants were added to target cells for a period of 24
521 hours prior to fixation with 4% paraformaldehyde (for measurements of GFP+ cells with flow
522 cytometry). For infections with replication-competent SARS-CoV-2, rapamycin, everolimus,
523 temsirolimus, or ridaforolimus (20 µM) were used to pretreat cells for 4 hours and then drugs were
524 washed away prior to addition of virus at a multiplicity of infection (MOI) of 0.1. DMSO (Sigma)
525 was used as a vehicle control. At one hour post-virus addition, cells were washed once with 1X
526 PBS and overlayed with complete medium. Supernatants were harvested 24 hours later, and titers
527 were determined on plaque assays performed in Vero E6 cells. For single-round infections using
528 HIV- or VSV-based pseudovirus, rapamycin, everolimus, temsirolimus, ridaforolimus, or
529 tacrolimus (20 µM) were used to pretreat cells for 4 hours and were maintained for the duration of
530 infection and until harvest of cells for luciferase assay or flow cytometry. DMSO (Sigma) was
531 used as a vehicle control.
532
533 **FRET-based virus entry assay**
534
535 HIV-based pseudovirus incorporating BlaM-Vpr and CoV-2 Spike was produced by transfecting
536 HEK293T cells with pNL4-3E- (15 µg), pCMV4-BlaM-Vpr (5 µg), and pcDNA3.1 CoV-2 Spike
537 (5 µg) using the calcium phosphate technique. Briefly, six million 293T cells were seeded in a T75
538 flask. Plasmid DNA was mixed with sterile H_2O, $CaCl_2$, and Tris-EDTA (TE) buffer, and the
539 totality was combined with Hepes-buffered saline (HBS). The transfection volume was added
540 dropwise, and cells were incubated at 37°C for 48 h. Supernatants were recovered and clarified by
541 centrifugation, passed through a 0.45 µm filter, and stored. Titers were measured using an HIV-1
542 p24 ELISA kit (XpressBio). 50 ng p25 equivalent of virus was added to HeLa-ACE2 cells for 2
543 hours. Cells were washed and labeled with the CCF2-AM β-lactamase Loading Kit (Invitrogen)
544 for 2 hours and analyzed for CCF2 cleavage by flow cytometry as described [88]. Rapamycin,
545 everolimus, temsirolimus, or ridaforolimus (20 µM) were used to pretreat cells for 4 hours prior
546 to virus addition and were maintained for the duration of infection. DMSO (Sigma) was used as a
547 vehicle control.
548
549 **Western blot, flow cytometry, and antibodies**

550 Whole cell lysis was performed with RIPA buffer (Thermo Fisher) supplemented with Halt
551 Protease Inhibitor EDTA-free (Thermo Fisher). Lysates were clarified by centrifugation and

552 supernatants were collected and stored. Protein concentration was determined with the Protein
553 Assay Kit II (Bio-Rad), and 10-15 µg of protein was loaded into 12% acrylamide Criterion XT
554 Bis-Tris Precast Gels (Bio-Rad). Electrophoresis was performed with NuPage MES SDS Running
555 Buffer (Invitrogen) and proteins were transferred to Amersham Protran Premium Nitrocellulose
556 Membrane, pore size 0.20 µm (GE Healthcare). Membranes were blocked with Odyssey Blocking
557 Buffer (Li-COR) and incubated with the following primary antibodies diluted in Odyssey
558 Antibody Diluent (Li-COR): anti-IFITM1 (60074-1-Ig; Proteintech), anti-IFITM2 (66137-1-Ig;
559 Proteintech), anti-IFITM3 (EPR5242, ab109429; Abcam), anti-IFITM2/3 (66081-1-Ig;
560 Proteintech), anti-actin (C4, sc-47778; Santa Cruz Biotechnology), anti-hACE2 (ab15348;
561 Abcam), anti-TFEB (4240S; Cell Signaling Technology), and anti-pTFEB (Ser211) (37681S; Cell
562 Signaling Technology). Secondary antibodies conjugated to DyLight 800 or 680 (Li-Cor) and the
563 Li-Cor Odyssey CLx imaging system were used to reveal specific protein detection. Images were
564 analyzed (including signal quantification) and assembled using ImageStudioLite (Li-Cor).

565 **Confocal fluorescence and immunofluorescence microscopy**
566
567 HeLa-ACE2 cells were fixed with 4% paraformaldehyde, stained with anti-IFITM2/3 (66081-1-
568 Ig; Proteintech), goat anti-mouse IgG Alexa Fluor 647 (A21235; Thermo Fisher) and DAPI
569 (62248; Thermo Fisher), and imaged in a glass-bottom tissue culture plate with an Operetta CLS
570 High-Content Analysis System (Perkin Elmer). For measurement of TFEB-GFP
571 nuclear/cytoplasmic distribution, HeLa-ACE2 cells were transfected with pEGFP-N1-TFEB for
572 24 hours, fixed with 4% paraformaldehyde, stained with HCS CellMask Red Stain (H32712;
573 Thermo Fisher) and DAPI, and imaged with an Operetta CLS. Using Harmony software (Perkin
574 Elmer), nuclear/cytoplasmic ratios of TFEB-GFP were calculated in single cells as follows: cells
575 were delineated by CellMask Red Stain, nuclei were delineated by DAPI, nuclear TFEB-GFP was
576 designated as GFP overlapping with DAPI, and cytoplasmic TFEB-GFP was designated as total
577 GFP signal minus nuclear TFEB-GFP. Average ratios were calculated from 20-30 cells per field,
578 and the mean of averages from 10 fields was obtained (total of approximately 250 cells per
579 condition). For measurement of IFITM2/3 levels in cells transfected with TFEBΔ30-GFP, HeLa-
580 ACE2 cells were transfected with pEGF-N1-Δ30TFEB for 24 hours, fixed and permeabilized with
581 BD Cytofix/Cytoperm (Fisher Scientific), stained with anti-IFITM2/3 and goat anti-mouse IgG
582 Alexa Fluor 647, and imaged with an Operetta CLS. The IFITM2/3 fluorescence intensity within
583 a single, medial Z section was measured in approximately 150 GFP-negative cells and 150 GFP-
584 positive cells using the freehand selections tool in ImageJ.

585 **Proteomics by mass spectrometry**
586
587 <u>Protein Digestion and TMT labeling.</u> Cell pellets were produced in triplicate from A549-ACE2
588 cells treated with 20 µM temsirolimus or ridaforolimus, or an equivalent volume of DMSO and
589 lysed in RIPA buffer followed by sonication. Lysates were clarified by centrifugation and protein
590 concentration was quantified using BCA protein estimation kit (Thermo Fisher). One hundred
591 micrograms of lysate were alkylated and digested by addition of trypsin at a ratio of 1:50
592 (Promega) and incubating overnight at 37ºC. Digestion was acidified by adding formic acid (FA)
593 to a final concentration of 1% and desalted using peptide desalting columns (Thermo Fisher)
594 according to manufacturer's protocol. Peptides were eluted from the columns using 50%
595 ACN/0.1% FA, dried in a speedvac, and kept frozen at -20ºC until further analysis. For TMT

596 labeling, 15 µg of each sample was reconstituted in 50 µL of 50 mM HEPES, pH 8.0, and 75 µg
597 of TMTpro label (Thermo Fisher) in 100% ACN was added to each sample. After incubating the
598 mixture for 1 hr at room temperature with occasional mixing, the reaction was terminated by
599 adding 8 µL of 5% hydroxylamine. The peptide samples for each condition were pooled and
600 cleaned using peptide desalting columns (Thermo Fisher). High pH reverse phase fractionation.
601 The first dimensional separation of the peptides was performed using a Waters Acquity UPLC
602 system coupled with a fluorescence detector (Waters) using a 150 mm x 3.0 mm Xbridge Peptide
603 BEM™ 2.5 um C18 column (Waters) operating at 0.35 mL/min. The dried peptides were
604 reconstituted in 100 µL of mobile phase A solvent (3 mM ammonium bicarbonate, pH 8.0). Mobile
605 phase B was 100% acetonitrile (Thermo Fisher). The column was washed with mobile phase A
606 for 10 min followed by gradient elution 0-50% B (10-60 min) and 50-75% B (60-70 min). The
607 fractions were collected every minute. These 60 fractions were pooled into 24 fractions. The
608 fractions were vacuum centrifuged to dryness and stored at -80ºC until analysis by mass
609 spectrometry. Mass Spectrometry acquisition and data analysis. The dried peptide fractions were
610 reconstituted in 0.1% TFA and subjected to nanoflow liquid chromatography (Thermo Ultimate™
611 3000RSLC nano LC system, Thermo Scientific) coupled to an Orbitrap Eclipse mass spectrometer
612 (Thermo Scientific). Peptides were separated using a low pH gradient using 5-50% ACN over 120
613 minutes in mobile phase containing 0.1% formic acid at 300 nL/min flow rate. MS scans were
614 performed in the Orbitrap analyzer at a resolution of 120,000 with an ion accumulation target set
615 at $4e^5$ and max IT set at 50ms over a mass range of 400-1600 m/z. Ions with determined charge
616 states between 2 and 5 were selected for MS2 scans in the ion trap with CID fragmentation (Turbo;
617 NCE 35%; maximum injection time 35 ms; AGC 1×10^4). The spectra were searched using the
618 Real Time Search Node in the tune file using human Uniprot database using Comet search
619 algorithm with TMT16 plex (304.2071Da) set as a static modification of lysine and the N-termini
620 of the peptide. Carbamidomethylation of cysteine residues (+57.0214 Da) was set as a static
621 modification, while oxidation of methionine residues (+15.9949 Da) was set up as dynamic
622 modification. For the selected peptide, an SPS–MS3 scan was performed using up to 10 *b*- and *y*-
623 type fragment ions as precursors in an Orbitrap at 50,000 resolution with a normalized AGC set at
624 500 followed by maximum injection time set as "Auto" with a normalized collision energy setting
625 of 65. Acquired MS/MS spectra were searched against a human Uniprot protein database along
626 with a contaminant protein database, using a SEQUEST and percolator validator algorithms in the
627 Proteome Discoverer 2.4 software (Thermo Scientific). The precursor ion tolerance was set at 10
628 ppm and the fragment ions tolerance was set at 0.02 Da along with methionine oxidation included
629 as dynamic modification. Carbamidomethylation of cysteine residues and TMT16 plex
630 (304.2071Da) was set as a static modification of lysine and the N-termini of the peptide. Trypsin
631 was specified as the proteolytic enzyme, with up to 2 missed cleavage sites allowed. Searches used
632 a reverse sequence decoy strategy to control for the false peptide discovery and identifications
633 were validated using percolator software. Reporter ion intensities were adjusted to correct for the
634 impurities according to the manufacturer's specification and the abundances of the proteins were
635 quantified using the summation of the reporter ions for all identified peptides. The reporter
636 abundances were normalized across all the channels to account for equal peptide loading. Median
637 abundance values for DMSO, temsirolimus, and ridaforolimus were calculated from three
638 replicates and presented as medians plus 95% confidence intervals.

639 **In vivo infections of hamsters and mice with SARS-CoV-2**
640

641 Male Golden Syrian hamsters between the ages of 6-8 weeks were acclimated for 11 days
642 following receipt. Hamsters received an intraperitoneal injection (500 µL) of rapamycin (HY-
643 10219; MedChemExpress) or ridaforolimus (HY-50908; MedChemExpress) at 3 mg/kg or an
644 equivalent amount of DMSO (4 hamsters per group). Four hours later, hamsters were challenged
645 with 6 x 10^3 plaque forming units of SARS-CoV-2 isolate USA-WA1/2020 (amplified on Calu-3
646 cells) through intranasal inoculation (50 µL in each nare). Clinical observations and weights were
647 recorded daily up until day 10 post-infection. According to Institutional Animal Care and Use
648 Committee human euthanasia criteria, hamsters were euthanized immediately if weight loss
649 exceeded 20%. Otherwise, hamsters were euthanized on day 10 post-infection. Oral swabs were
650 collected for measurement of viral RNA by quantitative PCR of the viral N (nucleocapsid) gene.
651 Lungs were harvested following euthanasia (day 10 or earlier) and infectious viral load was
652 determined by $TCID_{50}$ assay in Vero-TMPRSS2 cells. C57BL/6 mice received an intraperitoneal
653 injection of rapamycin (NC9362949; LC-Laboratories) or an equivalent amount of DMSO (7 and
654 6 mice per group, respectively). The following day, mice were challenged intranasally with 6 x
655 10^4 $TCID_{50}$ equivalent of MA10 SARS-CoV-2 (USA-WA1/2020 backbone). Mice received a
656 second injection of rapamycin or DMSO on the day of infection and a third on day one post-
657 infection. Mice were euthanized for lung harvest on day two post-infection. Infectious viral load
658 was determined by $TCID_{50}$ assay in Vero-TMPRSS2 cells. Animal studies were conducted in
659 compliance with all relevant local, state, and federal regulations and were approved by the
660 Institutional Animal Care and Use Committee of Bioqual and of the Ohio State University.
661
662 **Figure Legends**
663
664 **Figure 1: Rapamycin and its analogs share a macrolide structure but differ by the functional**
665 **group present at carbon-40.** Violet and green bubbles indicate the FKBP- and mTOR-binding
666 sites, respectively.

667 **Figure 2: Rapalogs promote SARS-CoV-2 infection in lung epithelial cells to different extents**
668 **by counteracting the intrinsic antiviral state** (A) A549-ACE2 were treated with or without type
669 I interferon (250 U/mL) for 18 hours and then treated with 20 µM rapamycin (Rap), everolimus
670 (Eve), temsirolimus (Tem), ridaforolimus (Rid), or an equivalent volume of DMSO (D) for 4
671 hours. HIV-CoV-2 (100 ng p24 equivalent) was added to cells and infection was measured by
672 luciferase activity at 48 hours post-infection. Luciferase units were normalized to 100 in the
673 DMSO condition in the absence of interferon. (B) A549-ACE2 cells from (A) were subjected to
674 SDS-PAGE and Western blot analysis. Immunoblotting was performed with anti-IFITM2/3, anti-
675 ACE2, and anti-actin (in that order) on the same nitrocellulose membrane. Numbers and tick marks
676 indicate size (kilodaltons) and position of protein standards in ladder. (C) Primary HSAEC were
677 treated with 20 µM Rap, Eve, Tem, Rid, or an equivalent volume of DMSO for 4 hours. VSV-
678 CoV-2 (50 µL) was added to cells and infection was measured by GFP expression at 24 hours
679 post-infection using flow cytometry. (D) A549-ACE2 were treated with varying concentrations of
680 Eve or DMSO for 4 hours. SARS-CoV-2 (nCoV-WA1-2020; MN985325.1) was added to cells at
681 an MOI of 0.1 and infectious titers were measured in VeroE6 cells by calculating the $TCID_{50}$ per
682 mL of supernatants recovered at 24 hours post-infection. $TCID_{50}$ per mL values were normalized
683 to 100 in the DMSO condition. Means and standard error were calculated from 3-5 experiments.
684 Statistical analysis was performed with one-way ANOVA and asterisks indicate significant
685 difference from DMSO. *, $p < 0.05$; **, $p < 0.01$. Rel.; relative.

686 **Figure 3: Rapalogs promote SARS-CoV-2 infection in HeLa-ACE2 cells.** (A) HeLa-ACE2
687 were treated with varying concentrations of Eve or DMSO for 4 hours. SARS-CoV-2 (nCoV-
688 WA1-2020; MN985325.1) was added to cells at an MOI of 0.1 and infectious titers were measured
689 in VeroE6 cells by calculating the $TCID_{50}$ of supernatants recovered at 24 hours post-infection.
690 $TCID_{50}$ per mL values were normalized to 100 in the DMSO condition. (B) HeLa-ACE2 were
691 treated with 20 µM Rap, Eve, Tem, Rid, or an equivalent volume of DMSO for 4 hours. SARS-
692 CoV-2 (nCoV-WA1-2020; MN985325.1) was added to cells at an MOI of 0.1 and infectious titers
693 were measured in VeroE6 cells by calculating the $TCID_{50}$ per mL of supernatants recovered at 24
694 hours post-infection. $TCID_{50}$ per mL values were normalized to 100 in the DMSO condition. (C)
695 HeLa-ACE2 were treated with 20 µM Rap, Eve, Tem, Rid, or an equivalent volume of DMSO for
696 4 hours. HIV-CoV-2 (100 ng p24 equivalent) was added to cells and infection was measured by
697 luciferase activity at 48 hours post-infection. Luciferase units were normalized to 100 in the
698 DMSO condition. (D) HeLa-ACE2 cells from (C) were subjected to SDS-PAGE and Western blot
699 analysis. Immunoblotting was performed with anti-IFITM2, anti-IFITM1, anti-IFITM3, anti-
700 ACE2, and anti-actin (in that order) on the same nitrocellulose membrane. (E) IFITM3 levels from
701 (D) were normalized to actin levels and summarized from 5 independent experiments. (F) HeLa-
702 ACE2 were treated with 20 µM Rap, Eve, Tem, Rid, or an equivalent volume of DMSO for 4
703 hours and cells were fixed, stained with DAPI and anti-IFITM2/3, and imaged by confocal
704 immunofluorescence microscopy. Images represent stacks of 5 Z-slices and one representative
705 image is shown per condition. Means and standard error were calculated from 3-5 experiments.
706 Statistical analysis was performed with one-way ANOVA and asterisks indicate significant
707 difference from DMSO. *, $p < 0.05$; **, $p < 0.01$. Rel.; relative.
708
709 **Figure 4: Rapalogs promote cell entry mediated by diverse viral fusion proteins.** (A) HeLa-
710 ACE2 were treated with 20 µM Rap, Eve, Tem, Rid, or an equivalent volume of DMSO for 4
711 hours. HIV-CoV-2 S pseudovirus incorporating BlaM-Vpr (HIV-BlaM-CoV-2) was added to cells
712 for 2 hours and washed. Cells were incubated with CCF2-AM for an additional 2 hours and fixed.
713 Cleaved CCF2 was measured by flow cytometry. Dot plots visualized as density plots from one
714 representative experiment are shown on the left and the percentage of CCF2+ cells which exhibit
715 CCF2 cleavage is indicated. Summary data representing the average of four experiments is shown
716 on the right. (B) HIV-CoV-1, (C) HIV-MERS-CoV, (D) HIV-IAV HA, or (E) HIV-VSV G were
717 added to HeLa-ACE2 or HeLa-DPP4 cells as in (A) and infection was measured by luciferase
718 activity at 48 hours post-infection. Luciferase units were normalized to 100 in the DMSO
719 condition. Means and standard error were calculated from 3-4 experiments. Statistical analysis was
720 performed with one-way ANOVA and asterisks indicate significant difference from DMSO. *, p
721 < 0.05; **, $p < 0.01$. Rel.; relative.
722
723 **Figure 5: Enhancement of infection by select rapalogs is associated with inhibition of mTOR-**
724 **mediated phosphorylation of TFEB in lung cells.** (A) A549-ACE2 were treated with 20 µM
725 Rap, Eve, Tem, Rid, or tacrolimus (Tac) for 4 hours and whole cell lysates were subjected to SDS-
726 PAGE and Western blot analysis. Immunoblotting was performed with anti-TFEB and anti-pTFEB
727 (S211). (B) pTFEB (S211) levels were divided by total TFEB levels and summarized as an average
728 of 3 experiments. Means and standard error are shown. Statistical analysis was performed with
729 one-way ANOVA and asterisks indicate significant difference from DMSO. (C) A549-ACE2 cells
730 were treated with 20 µM Tem, Rid, or an equivalent volume of DMSO for 4 hours and proteins
731 were extracted for analysis by mass spectrometry. Raw data in triplicate of all proteins detected is

presented in Supplemental File 1. Median protein levels for five genes known to be regulated by TFEB are shown. ACE2 is also shown for comparison. Statistical analysis was performed with a student's T test and asterisks indicate significant difference from DMSO. *, $p < 0.05$ or $p = 0.05$; **, $p < 0.01$. Rel.; relative.

Figure 6: Enforced localization of ectopic TFEB triggers IFITM2/3 turnover and promotes Spike-mediated infection. (A) HeLa-ACE2 were treated with 20 µM Tem, Rid, or Tac for 4 hours and whole cell lysates were subjected to SDS-PAGE and Western blot analysis. Immunoblotting was performed with anti-TFEB and anti-pTFEB (S211). (B) pTFEB (S211) levels were divided by total TFEB levels and summarized as an average of 3 experiments. (C) HeLa-ACE2 were transfected with TFEB-GFP for 24 hours, treated with Tem, Rid or Tac for 4 hours, stained with DAPI and CellMask, and imaged by high-content confocal fluorescence microscopy. Representative images from each condition are shown on the left. The ratio of nuclear to cytoplasmic TFEB-GFP was calculated in individual cells and the average ratio derived from approximately 200-300 cells per condition is shown to the right. (E) HeLa-ACE2 were transfected with 0.5 µg TFEBΔ30-GFP for 24 hours, fixed, stained with anti-IFITM2/3, and imaged by confocal immunofluorescence microscopy. (F) The average intensity of IFITM2/3 levels in approximately 150 GFP-negative and 150 GFP-positive cells is grouped and summarized from two independent transfections. (G) HeLa-ACE2 were transfected with 0.5 µg TFEBΔ30-GFP for 24 hours and HIV-CoV-2 (100 ng p24 equivalent) was added to cells. Infection was measured by luciferase activity at 48 hours post-infection. Luciferase units were normalized to 100 in the non-transfected condition. Means and standard error were calculated from 3 experiments, except for TFEB-GFP imaging experiments, for which 2 experiments (transfections) were performed. Statistical analysis was performed with one-way ANOVA and asterisks indicate significant difference from Tac. *, $p < 0.05$; **, $p < 0.01$. Rel.; relative.

Figure 7: Rapamycin injection into rodents prior to challenge with SARS-CoV-2 intensifies viral disease. (A) Schematic of intraperitoneal injections and intranasal SARS-CoV-2 challenge in hamsters. Golden Syrian hamsters were injected with 3 mg/kg Rap, Rid, or equivalent amounts of DMSO (4 animals per group). Four hours later, hamsters were infected intranasally with 6×10^3 plaque forming units of SARS-CoV-2. At 2 days post-infection, oral swabs were taken and used for measurement of oral viral RNA load by qPCR. At 10 days post-infection (or earlier, if more than 20% of weight loss occurred), hamsters were euthanized, and lungs were harvested for determination of infectious virus titer by $TCID_{50}$ assay in Vero-TMPRSS2 cells (B) Mean body weight and standard error for each treatment group is plotted by day post-infection. (C) Kaplan-Meier survival curves were generated according to the dates of euthanasia (or in one case, when an animal was found dead). (D) Viral RNA copy number was determined by qPCR from oral swab at 2 days post-infection. Data is depicted as box and whiskers plots. (E) Infectious virus titers in lungs were determined by $TCID_{50}$ in Vero-TMPRSS2 cells. Data is depicted as floating bars and is grouped by brackets according to hamsters that survived until 10 days post-infection and those that were euthanized at 7 days post-infection. Statistical analysis in (B) was performed by student's T test and asterisks indicate significant difference from DMSO (gray asterisks for Rap and black asterisks for Rid). Statistical analysis in (C) was performed by comparing survival curves between Rap and DMSO or Rid and DMSO using the Log-rank (Mantel-Cox) test. (F) Schematic of intraperitoneal injections and intranasal mouse-adapted (MA) SARS-CoV-2 challenge in mice. C57BL/6 mice were injected with 3 mg/kg of Rap or an equivalent amount of DMSO (6 or 7 mice

778 per group, respectively). The following day, mice were infected intranasally with 6 x 10^4 $TCID_{50}$
779 MA SARS-CoV-2. Mice received second and third injections of Rap or DMSO on the day of
780 infection and day one post-infection, respectively. (G) Lungs were harvested from infected mice
781 upon euthanasia at day 2 post-infection and infectious viral loads were determined by $TCID_{50}$ in
782 Vero-TMPRSS2 cells. Geometric mean $TCID_{50}$ per gram was calculated per treatment group and
783 data is depicted as box and whiskers plots. Statistical analysis was performed with Mann-Whitney
784 test and asterisks indicate significant difference from DMSO. *, $p < 0.05$; **, $p < 0.01$. Illustration
785 created with BioRender.com.
786
787 **Figure 8:** Model for rapalog-mediated enhancement of SARS-CoV-2 infection. Rapamycin and
788 rapalogs everolimus and temsirolimus potently inhibit the phosphorylation of TFEB by mTOR,
789 while ridaforolimus does not. As a result, TFEB translocates into the nucleus and induces genes
790 functioning in lysosomal activities, including autophagy-related pathways. Nuclear TFEB triggers
791 a microautophagy pathway that results in accelerated degradation of membrane proteins IFITM2
792 and IFITM3. Loss of IFITM2/3 promotes SARS-CoV-2 entry into cells by facilitating fusion
793 between viral membranes and cellular membranes. Illustration created with BioRender.com.

794 **Supplemental Figure 1:** (A) Primary HSAEC were treated with 20 μM Rap, Eve, Tem, Rid, or
795 an equivalent volume of DMSO for 4 hours and whole cell lysates were subjected to SDS-PAGE
796 and Western blot analysis. Immunoblotting was performed with anti-IFITM2 (not detected), anti-
797 IFITM3, anti-IFITM1, and anti-actin. (B) Primary HSAEC were transfected with siRNA targeting
798 IFITM3 or control siRNA for 48 hours. VSV-CoV-2 (50 μL) was added to cells and infection was
799 measured by GFP expression at 24 hours post-infection using flow cytometry. siRNA-transfected
800 cells were subjected to SDS-PAGE and Western blot analysis. Immunoblotting was performed
801 with anti-IFITM2 (not detected), anti-IFITM3, anti-IFITM1, and anti-actin. (C) Semi-transformed
802 nasal epithelial cells (UNCNN2TS) were treated with 20 μM Rap, Eve, Tem, Rid, or an equivalent
803 volume of DMSO for 4 hours and whole cell lysates were subjected to SDS-PAGE and Western
804 blot analysis. Immunoblotting was performed with anti-IFITM2 (not detected), anti-IFITM3, anti-
805 IFITM1, and anti-actin. Immunoblots are representative of 3 independent experiments. Means and
806 standard error were calculated from 3 experiments. Statistical analysis was performed with
807 student's T test and asterisks indicate significant difference from control siRNA. *, $p < 0.05$; **,
808 $p < 0.01$. Rel.; relative.

809 **Supplemental Figure 2:** (A) HeLa-ACE2 were treated with 20 μM Rap, Eve, Tem, Rid, or an
810 equivalent volume of DMSO for 24 hours and whole cell lysates were subjected to SDS-PAGE
811 and Western blot analysis. Immunoblotting was performed with anti-IFITM2/3 and anti-actin. (B)
812 HeLa-ACE2 were treated with 20 μM Rap, Eve, Tem, Rid, or an equivalent volume of DMSO in
813 the presence or absence of 1 μM Bafilomycin A1 for 4 hours and whole cell lysates were subjected
814 to SDS-PAGE and Western blot analysis. Immunoblotting was performed with anti-IFITM2, anti-
815 IFITM1, anti-IFITM3, and anti-actin (in that order) on the same nitrocellulose membrane. (C)
816 HeLa-ACE2 cells were transected with FYVE-GFP for 24 hours followed by treatment with 100
817 nM SAR405 or an equivalent volume of ethanol (vehicle) for 3 hours. Cells were fixed and imaged
818 by confocal immunofluorescence microscopy. For each condition, a Z-stack of 25 slices is shown
819 as a maximum intensity projection. (D) HeLa-ACE2 were treated with 20 μM Rap, Eve, Tem, Rid,
820 or an equivalent volume of DMSO in the presence or absence of 100 nM SAR405 for 4 hours and
821 whole cell lysates were subjected to SDS-PAGE and Western blot analysis. Immunoblotting was

822 performed with anti-IFITM2/3 and anti-actin on the same nitrocellulose membrane. All
823 immunoblots are representative of three independent experiments.
824
825 **Supplemental Figure 3:** (A) HeLa WT and HeLa *IFITM1-3* KO cells were transiently transfected
826 with ACE2 for 24 hours. Whole cell lysates were subjected to SDS-PAGE and Western blot
827 analysis. Immunoblotting was performed with anti-IFITM2, anti-IFITM3, anti-IFITM1, anti-
828 ACE2, and anti-actin (in that order) on the same nitrocellulose membrane. (B) HeLa *IFITM1-3*
829 KO were transfected with IFITM2 or IFITM2 and IFITM3 and SDS-PAGE and Western blot
830 analysis was performed. (C) HIV-CoV-2 was added to transfected cells from (B) and infection was
831 measured by luciferase activity at 48 hours post-infection. Luciferase units were normalized to 100
832 in HeLa WT cells treated with DMSO. Means and standard error were calculated from 5
833 experiments. Statistical analysis was performed with one-way ANOVA and asterisks indicate
834 significant difference from nearest DMSO condition. *, $p < 0.05$; **, $p < 0.01$. Rel.; relative.
835
836 **Supplemental Figure 4:** (A) HeLa-ACE2 were treated with 20 μM Rap, Eve, Tem, Rid, or Tac
837 for 4 hours and whole cell lysates were subjected to SDS-PAGE and Western blot analysis.
838 Immunoblotting was performed with anti-IFITM2/3 and anti-actin. (B) HIV-CoV-2 was added to
839 HeLa-ACE2 treated as in (A) and infection was measured by luciferase activity at 48 hours post-
840 infection. Luciferase units were normalized to 100 in the DMSO condition.

841 **Supplemental File 1:** Spreadsheet of proteomics data obtained by mass spectrometry.

842 **Acknowledgements**
843
844 We thank Michael Letko and Vincent Munster for providing VSV-luc/GFP seed particles
845 and CoV and CoV-2 Spike plasmids, Thomas Gallagher for providing CoV, CoV-2, and MERS
846 Spike plasmids, Alan Rein for facilitating lentiviral pseudovirus production, Scott H. Randell for
847 providing UNCNN2TS, and Eric O. Freed for providing primary HSAEC.
848
849 **Funding sources**
850
851 Work in the lab of AAC was funded by the Intramural Research Program, National
852 Institutes of Health, National Cancer Institute, Center for Cancer Research and an Intramural
853 Targeted Anti-COVID-19 award from the National Institute of Allergy and Infectious Diseases.
854 Work in the lab of SMB was funded by the Division of Intramural Research, National Institutes of
855 Health, National Institute of Allergy and Infectious Diseases. Work in the lab of JSY was funded
856 by National Institutes of Health grants AI130110, AI151230, AI142256, and HL154001.
857
858 **References**
859
860 1. Zhu, N., et al., *A Novel Coronavirus from Patients with Pneumonia in China, 2019.* New
861 England Journal of Medicine, 2020. **382**(8): p. 727-733.
862 2. Wu, F., et al., *A new coronavirus associated with human respiratory disease in China.*
863 Nature, 2020: p. 1-20.
864 3. Zhang, X., et al., *Viral and host factors related to the clinical outcome of COVID-19.*
865 Nature, 2020: p. 1-18.

4. Aydillo, T., N.E. Babady, and M. Kamboj, *Shedding of Viable SARS-CoV-2 after Immunosuppressive Therapy for Cancer.* New England Journal of Medicine, 2020. **383**(26): p. 2586-2588.
5. Wei, J., et al., *SARS-CoV-2 infection in immunocompromised patients: humoral versus cell-mediated immunity.* Journal for immunotherapy of cancer, 2020. **8**(2): p. e000862.
6. Tarhini, H., et al., *Long term SARS-CoV-2 infectiousness among three immunocompromised patients: from prolonged viral shedding to SARS-CoV-2 superinfection.* The Journal of Infectious Diseases, 2021.
7. Baang, J.H., et al., *Prolonged Severe Acute Respiratory Syndrome Coronavirus 2 Replication in an Immunocompromised Patient.* The Journal of Infectious Diseases, 2021. **223**(1): p. 23-27.
8. Avanzato, V.A., et al., *Case Study: Prolonged Infectious SARS-CoV-2 Shedding from an Asymptomatic Immunocompromised Individual with Cancer.* Cell, 2020. **183**(7): p. 1901-1912.e9.
9. Gordon, D.E., et al., *A SARS-CoV-2 protein interaction map reveals targets for drug repurposing.* Nature, 2020: p. 1-30.
10. Zhou, Y., et al., *Network-based drug repurposing for novel coronavirus 2019-nCoV/SARS-CoV-2.* Cell Discovery, 2020: p. 1-18.
11. Appelberg, S., et al., *Dysregulation in Akt/mTOR/HIF-1 signaling identified by proteo-transcriptomics of SARS-CoV-2 infected cells.* Emerging Microbes & Infections, 2020. **9**(1): p. 1748-1760.
12. Blagosklonny, M.V., *From causes of aging to death from COVID-19.* Aging, 2020. **12**(11): p. 10004-10021.
13. Ciliberto, G., R. Mancini, and M.G. Paggi, *Drug repurposing against COVID-19: focus on anticancer agents.* 2020: p. 1-9.
14. Husain, A. and S.N. Byrareddy, *Rapamycin as a potential repurpose drug candidate for the treatment of COVID-19.* Chemico-Biological Interactions, 2020. **331**: p. 109282.
15. Zheng, Y., R. Li, and S. Liu, *Immunoregulation with mTOR inhibitors to prevent COVID-19 severity: A novel intervention strategy beyond vaccines and specific antiviral medicines.* Journal of medical virology, 2020. **92**(9): p. 1495-1500.
16. Terrazzano, G., et al., *An Open Question: Is It Rational to Inhibit the mTor-Dependent Pathway as COVID-19 Therapy?* 2020: p. 1-5.
17. Ramaiah, M.J., *mTOR inhibition and p53 activation, microRNAs: The possible therapy against pandemic COVID-19.* Gene reports, 2020. **20**: p. 100765.
18. Zhavoronkov, A., *Geroprotective and senoremediative strategies to reduce the comorbidity, infection rates, severity, and lethality in gerophilic and gerolavic infections.* Aging, 2020. **12**(8): p. 6492-6510.
19. Willyard, C., *Ageing and Covid Vaccines.* Nature, 2020. **586**(7829): p. 352-354.
20. Omarjee, L., et al., *Targeting T-cell senescence and cytokine storm with rapamycin to prevent severe progression in COVID-19.* Clinical immunology (Orlando, Fla.), 2020. **216**: p. 108464.
21. Laplante, M. and D.M. Sabatini, *mTOR signaling in growth control and disease.* Cell, 2012. **149**(2): p. 274-293.
22. Bertram, P.G., et al., *The 14-3-3 proteins positively regulate rapamycin-sensitive signaling.* Current biology : CB, 1998. **8**(23): p. 1259-1267.

23. Vignot, S., et al., *mTOR-targeted therapy of cancer with rapamycin derivatives.* Annals of Oncology, 2005. **16**(4): p. 525-537.
24. Lamming, D.W., et al., *Rapalogs and mTOR inhibitors as anti-aging therapeutics.* Journal of Clinical Investigation, 2013. **123**(3): p. 980-989.
25. Abdel-Magid, A.F., *Rapalogs Potential as Practical Alternatives to Rapamycin.* ACS medicinal chemistry letters, 2019. **10**(6): p. 843-845.
26. Benjamin, D., et al., *Rapamycin passes the torch: a new generation of mTOR inhibitors.* Nature Reviews Drug Discovery, 2011: p. 1-13.
27. Marz, A.M., et al., *Large FK506-Binding Proteins Shape the Pharmacology of Rapamycin.* Molecular and Cellular Biology, 2013. **33**(7): p. 1357-1367.
28. Zoncu, R., A. Efeyan, and D.M. Sabatini, *mTOR: from growth signal integration to cancer, diabetes and ageing.* Nature Reviews in Molecular Cell Biology, 2011. **12**(1): p. 21-35.
29. Chi, H., *Regulation and function of mTOR signalling in T cell fate decisions.* Nature Reviews Immunology, 2012: p. 1-14.
30. Mangalmurti, N. and C.A. Hunter, *Cytokine Storms: Understanding COVID-19.* Immunity, 2020. **53**(1): p. 19-25.
31. Mehta, P., et al., *COVID-19: consider cytokine storm syndromes and immunosuppression.* Lancet (London, England), 2020. **395**(10229): p. 1033-1034.
32. Manjili, R.H., et al., *COVID-19 as an Acute Inflammatory Disease.* The Journal of Immunology, 2020. **205**(1): p. 12-19.
33. Bischof, E., et al., *The potential of rapalogs to enhance resilience against SARS-CoV-2 infection and reduce the severity of COVID-19.* The Lancet. Healthy longevity, 2021. **2**(2): p. e105-e111.
34. Mullen, P.J., et al., *SARS-CoV-2 infection rewires host cell metabolism and is potentially susceptible to mTORC1 inhibition.* Nature communications, 2021: p. 1-10.
35. Alsuwaidi, A.R., et al., *Sirolimus alters lung pathology and viral load following influenza A virus infection.* Respiratory research, 2017. **18**(1): p. 136.
36. Huang, C.-T., et al., *Rapamycin adjuvant and exacerbation of severe influenza in an experimental mouse model.* Scientific Reports, 2017. **7**(1): p. 873-8.
37. Shi, G., et al., *mTOR inhibitors lower an intrinsic barrier to virus infection mediated by IFITM3.* Proceedings of the National Academy of Sciences of the United States of America, 2018. **115**(43): p. E10069-E10078.
38. Ozog, S., et al., *Resveratrol trimer enhances gene delivery to hematopoietic stem cells by reducing antiviral restriction at endosomes.* Blood, 2019. **134**(16): p. 1298-1311.
39. Shi, G., O. Schwartz, and A.A. Compton, *More than meets the I: the diverse antiviral and cellular functions of interferon-induced transmembrane proteins.* Retrovirology, 2017. **14**(1): p. 1-11.
40. Majdoul, S. and A.A. Compton, *Lessons in self-defence: inhibition of virus entry by intrinsic immunity.* Nature Reviews Immunology, 2021.
41. Bestle, D., et al., *TMPRSS2 and furin are both essential for proteolytic activation of SARS-CoV-2 in human airway cells.* Life science alliance, 2020. **3**(9): p. e202000786.
42. Hoffmann, M., H. Kleine-Weber, and S. Pöhlmann, *A Multibasic Cleavage Site in the Spike Protein of SARS-CoV-2 Is Essential for Infection of Human Lung Cells.* Molecular Cell, 2020. **78**(4): p. 779-784.e5.
43. Hoffmann, M., et al., *SARS-CoV-2 Cell Entry Depends on ACE2 and TMPRSS2 and Is Blocked by a Clinically Proven Protease Inhibitor.* Cell, 2020: p. 1-19.

957 44. Shi, G., et al., *mTOR inhibitors lower an intrinsic barrier to virus infection mediated by*
958 *IFITM3.* Proceedings of the National Academy of Sciences of the United States of
959 America, 2018. **115**(43): p. E10069-E10078.
960 45. Ronan, B., et al., *A highly potent and selective Vps34 inhibitor alters vesicle trafficking*
961 *and autophagy.* Nature chemical biology, 2014. **10**(12): p. 1-9.
962 46. Kolos, J.M., et al., *FKBP Ligands-Where We Are and Where to Go?* Frontiers in
963 pharmacology, 2018. **9**: p. 1425.
964 47. Roczniak-Ferguson, A., et al., *The transcription factor TFEB links mTORC1 signaling to*
965 *transcriptional control of lysosome homeostasis.* Science signaling, 2012. **5**(228): p. ra42.
966 48. Martina, J.A., et al., *MTORC1 functions as a transcriptional regulator of autophagy by*
967 *preventing nuclear transport of TFEB.* Autophagy, 2012. **8**(6): p. 903-14.
968 49. Settembre, C., et al., *A lysosome-to-nucleus signalling mechanism senses and regulates the*
969 *lysosome via mTOR and TFEB.* The EMBO journal, 2012. **31**(5): p. 1095-1108.
970 50. Zhang, X., et al., *Rapamycin directly activates lysosomal mucolipin TRP channels*
971 *independent of mTOR.* PLoS Biology, 2019. **17**(5): p. e3000252-24.
972 51. Palmieri, M., et al., *Characterization of the CLEAR network reveals an integrated control*
973 *of cellular clearance pathways.* Hum Mol Genet, 2011. **20**(19): p. 3852-66.
974 52. Di Fruscio, G., et al., *Lysoplex: An efficient toolkit to detect DNA sequence variations in*
975 *the autophagy-lysosomal pathway.* Autophagy, 2015. **11**(6): p. 928-38.
976 53. Alsuwaidi, A.R., et al., *Sirolimus alters lung pathology and viral load following influenza*
977 *A virus infection.* Respiratory research, 2017. **18**(1): p. 1-8.
978 54. Tostanoski, L.H., et al., *Ad26 vaccine protects against SARS-CoV-2 severe clinical disease*
979 *in hamsters.* Nat Med, 2020. **26**(11): p. 1694-1700.
980 55. Sasongko, T.H., et al., *Rapamycin and its analogues (rapalogs) for Tuberous Sclerosis*
981 *Complex-associated tumors: a systematic review on non-randomized studies using meta-*
982 *analysis.* Orphanet Journal of Rare Diseases, 2015: p. 1-11.
983 56. Reagan-Shaw, S., M. Nihal, and N. Ahmad, *Dose translation from animal to human studies*
984 *revisited.* FASEB J, 2008. **22**(3): p. 659-61.
985 57. Cloughesy, T.F., et al., *Antitumor activity of rapamycin in a Phase I trial for patients with*
986 *recurrent PTEN-deficient glioblastoma.* PLoS Med, 2008. **5**(1): p. e8.
987 58. Sun, Y., et al., *Phase II study of the safety and efficacy of temsirolimus in East Asian*
988 *patients with advanced renal cell carcinoma.* Jpn J Clin Oncol, 2012. **42**(9): p. 836-44.
989 59. Medina, D.L., et al., *Lysosomal calcium signalling regulates autophagy through*
990 *calcineurin and TFEB.* Nature Cell Biology, 2015. **17**(3): p. 288-299.
991 60. Schuck, S., *Microautophagy - distinct molecular mechanisms handle cargoes of many*
992 *sizes.* Journal of Cell Science, 2020. **133**(17).
993 61. Oku, M. and Y. Sakai, *Three Distinct Types of Microautophagy Based on Membrane*
994 *Dynamics and Molecular Machineries.* BioEssays, 2018. **40**(6): p. 1800008-6.
995 62. Santambrogio, L. and A.M. Cuervo, *Chasing the elusive mammalian microautophagy.*
996 Autophagy, 2011. **7**(6): p. 652-4.
997 63. Tekirdag, K. and A.M. Cuervo, *Chaperone-mediated autophagy and endosomal*
998 *microautophagy: Jointed by a chaperone.* Journal of Biological Chemistry, 2018. **293**(15):
999 p. 5414-5424.
1000 64. Mijaljica, D., M. Prescott, and R.J. Devenish, *Microautophagy in mammalian cells:*
1001 *revisiting a 40-year-old conundrum.* Autophagy, 2011. **7**(7): p. 673-682.

1002 65. Sato, M., et al., *Rapamycin activates mammalian microautophagy.* Journal of
1003 Pharmacological Science, 2019. **140**(2): p. 201-204.
1004 66. Yang, X., et al., *TORC1 regulates vacuole membrane composition through ubiquitin- and*
1005 *ESCRT-dependent microautophagy.* The Journal of Cell Biology, 2020. **219**(3).
1006 67. Li, M., et al., *Ubiquitin-Dependent Lysosomal Membrane Protein Sorting and*
1007 *Degradation.* Molecular Cell, 2015. **57**(3): p. 467-478.
1008 68. Chesarino, N.M., T.M. McMichael, and J.S. Yount, *E3 Ubiquitin Ligase NEDD4 Promotes*
1009 *Influenza Virus Infection by Decreasing Levels of the Antiviral Protein IFITM3.* PLoS
1010 Pathogens, 2015. **11**(8): p. e1005095.
1011 69. Compton, A.A., et al., *Natural mutations in IFITM3 modulate post-translational*
1012 *regulation and toggle antiviral specificity.* EMBO reports, 2016. **17**(11): p. 1657-1671.
1013 70. Yang, X., et al., *TORC1 regulates vacuole membrane composition through ubiquitin- and*
1014 *ESCRT-dependent microautophagy.* 2019. **8**: p. 1835-53.
1015 71. Zhao, X., et al., *Interferon induction of IFITM proteins promotes infection by human*
1016 *coronavirus OC43.* Proceedings of the National Academy of Sciences, 2014. **111**(18): p.
1017 6756-6761.
1018 72. Shi, G., et al., *Opposing activities of IFITM proteins in SARS-CoV-2 infection.* The EMBO
1019 journal, 2020. **3**: p. e201900542-12.
1020 73. Winstone, H., et al., *The polybasic cleavage site in the SARS-CoV-2 spike modulates viral*
1021 *sensitivity to Type I interferon and IFITM2.* Journal of Virology, 2021.
1022 74. Zhao, X., et al., *LY6E Restricts Entry of Human Coronaviruses, Including Currently*
1023 *Pandemic SARS-CoV-2.* Journal of Virology, 2020. **94**(18).
1024 75. Zang, R., et al., *Cholesterol 25-hydroxylase suppresses SARS-CoV-2 replication by*
1025 *blocking membrane fusion.* Proceedings of the National Academy of Sciences of the United
1026 States of America, 2020. **32**: p. 202012197.
1027 76. Huang, I.C., et al., *Distinct patterns of IFITM-mediated restriction of filoviruses, SARS*
1028 *coronavirus, and influenza A virus.* PLoS Pathogens, 2011. **7**(1): p. e1001258.
1029 77. Zhao, X., et al., *Identification of Residues Controlling Restriction versus Enhancing*
1030 *Activities of IFITM Proteins on Entry of Human Coronaviruses.* Journal of Virology, 2018.
1031 **92**(6): p. 374-17.
1032 78. Bozzo, C.P., et al., *IFITM proteins promote SARS-CoV-2 infection of human lung cells.*
1033 bioRxiv, 2020. **1**: p. 261-47.
1034 79. Beyer, D.K. and A. Forero, *Mechanisms of Antiviral Immune Evasion of SARS-CoV-2.* J
1035 Mol Biol, 2021: p. 167265.
1036 80. Hachim, M.Y., et al., *Interferon-Induced Transmembrane Protein (IFITM3) Is*
1037 *Upregulated Explicitly in SARS-CoV-2 Infected Lung Epithelial Cells.* Frontiers in
1038 Immunology, 2020. **11**: p. 1372.
1039 81. Blanco-Melo, D., et al., *Imbalanced Host Response to SARS-CoV-2 Drives Development*
1040 *of COVID-19.* Cell, 2020. **181**(5): p. 1036-1045.e9.
1041 82. Ziegler, C.G.K., et al., *Impaired local intrinsic immunity to SARS-CoV-2 infection in severe*
1042 *COVID-19.* bioRxiv, 2021: p. 2021.02.20.431155.
1043 83. Zhang, Y., et al., *Interferon-induced transmembrane protein-3 genetic variant rs12252-*
1044 *C is associated with disease severity in COVID-19.* The Journal of Infectious Diseases,
1045 2020.
1046 84. Nikoloudis, D., D. Kountouras, and A. Hiona, *The frequency of combined IFITM3*
1047 *haplotype involving the reference alleles of both rs12252 and rs34481144 is in line with*

1048 *COVID-19 standardized mortality ratio of ethnic groups in England.* PeerJ, 2020. **8**: p.
1049 e10402.
1050 85. Leist, S.R., et al., *A Mouse-Adapted SARS-CoV-2 Induces Acute Lung Injury and Mortality*
1051 *in Standard Laboratory Mice.* Cell, 2020. **183**(4): p. 1070-1085 e12.
1052 86. Chiramel, A.I., et al., *TRIM5α Restricts Flavivirus Replication by Targeting the Viral*
1053 *Protease for Proteasomal Degradation.* CellReports, 2019. **27**(11): p. 3269-3283.e6.
1054 87. Letko, M., A. Marzi, and V. Munster, *Functional assessment of cell entry and receptor*
1055 *usage for SARS-CoV-2 and other lineage B betacoronaviruses.* Nature Microbiology,
1056 2020. **11**: p. 1-17.
1057 88. Compton, A.A., et al., *IFITM Proteins Incorporated into HIV-1 Virions Impair Viral*
1058 *Fusion and Spread.* Cell Host & Microbe, 2014. **16**(6): p. 736-747.
1059

Figure 1

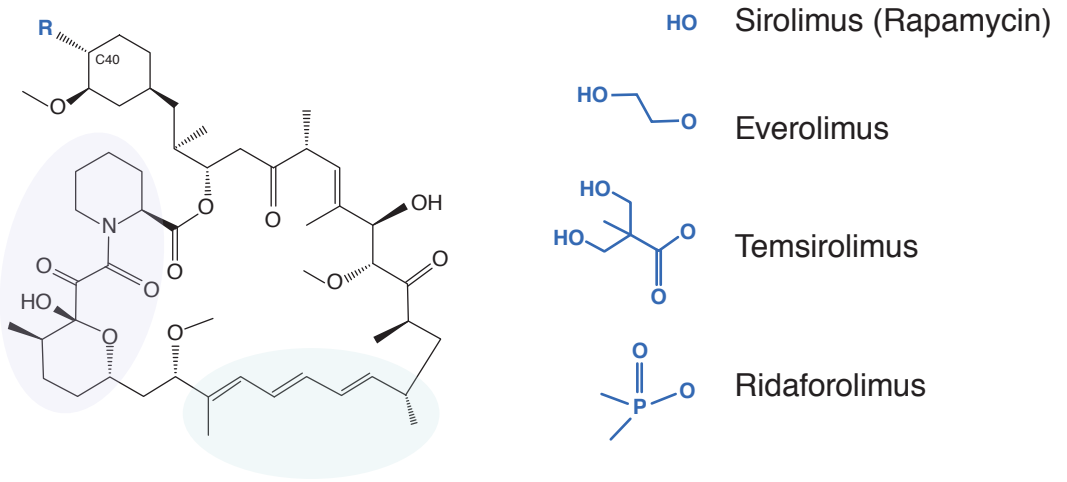
R
C40
O
N
O
O
O
OH
O
O
O
O
HO
O
O
HO
Sirolimus (Rapamycin)
HO
O
Everolimus
HO
HO
O
O
Temsirolimus
O
P
O
Ridaforolimus

Figure 2

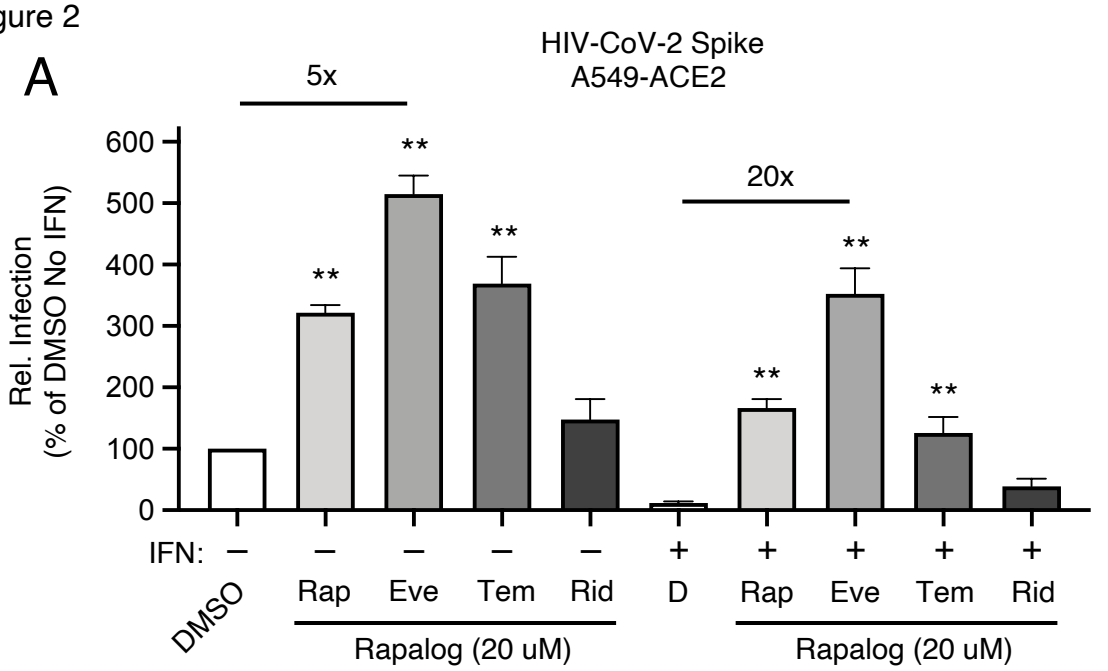
A
HIV-CoV-2 Spike
A549-ACE2
5x
20x
Rel. Infection
(% of DMSO No IFN)
600
500
400
300
200
100
0
**
IFN: – – – – – + + + + +
DMSO
Rap Eve Tem Rid
D Rap Eve Tem Rid
Rapalog (20 uM)
Rapalog (20 uM)

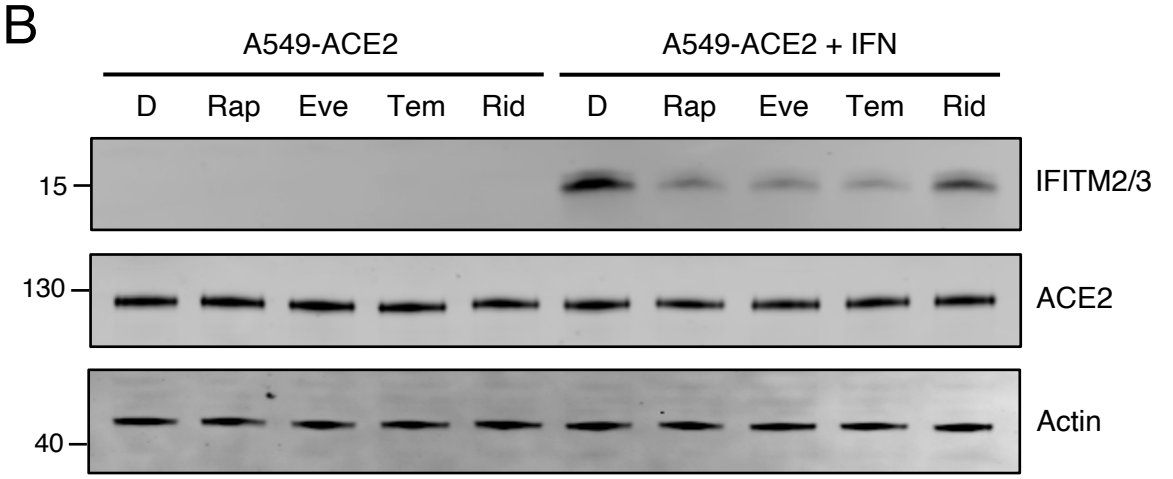
B
A549-ACE2
A549-ACE2 + IFN
D Rap Eve Tem Rid D Rap Eve Tem Rid
15
130
40
IFITM2/3
ACE2
Actin

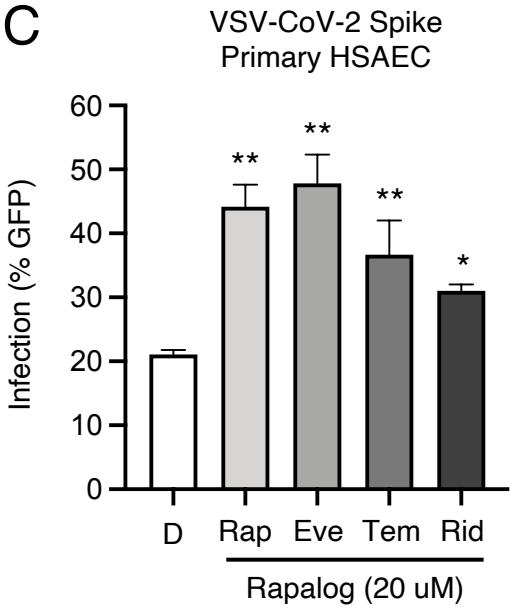
C
VSV-CoV-2 Spike
Primary HSAEC
Infection (% GFP)
60
50
40
30
20
10
0
**
*
D Rap Eve Tem Rid
Rapalog (20 uM)

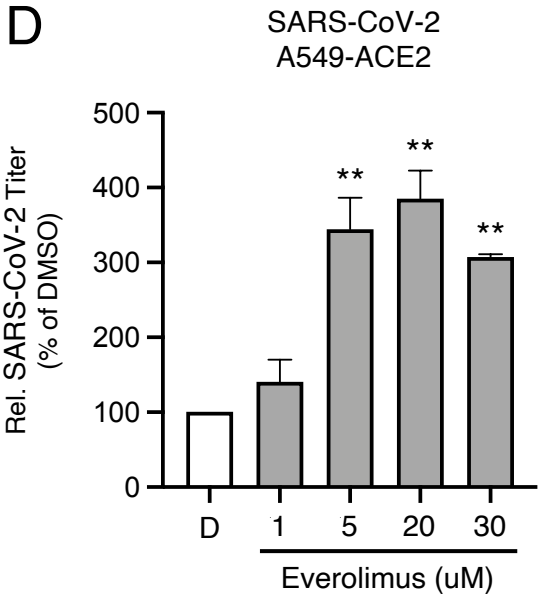
D
SARS-CoV-2
A549-ACE2
Rel. SARS-CoV-2 Titer
(% of DMSO)
500
400
300
200
100
0
**
D 1 5 20 30
Everolimus (uM)

Figure 3

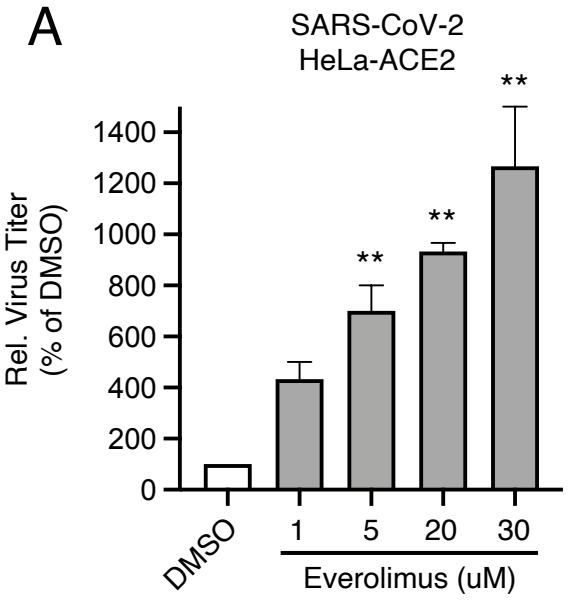
A
SARS-CoV-2
HeLa-ACE2
Rel. Virus Titer
(% of DMSO)
1400
1200
1000
800
600
400
200
0
**
**
**
DMSO
1
5
20
30
Everolimus (uM)

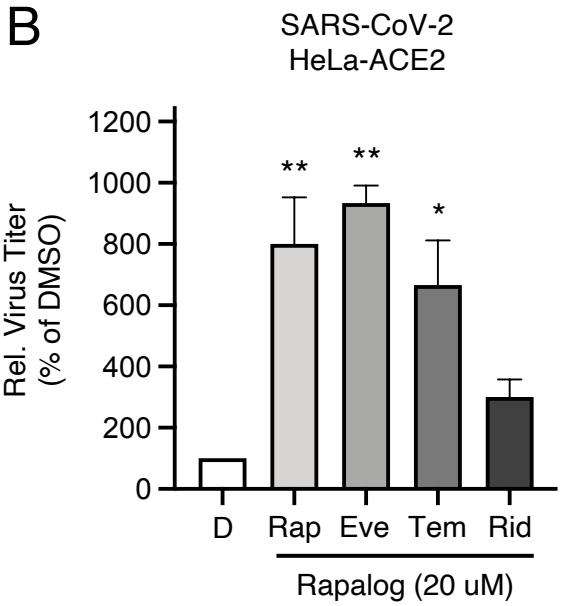
B
SARS-CoV-2
HeLa-ACE2
Rel. Virus Titer
(% of DMSO)
1200
1000
800
600
400
200
0
**
**
*
D
Rap
Eve
Tem
Rid
Rapalog (20 uM)

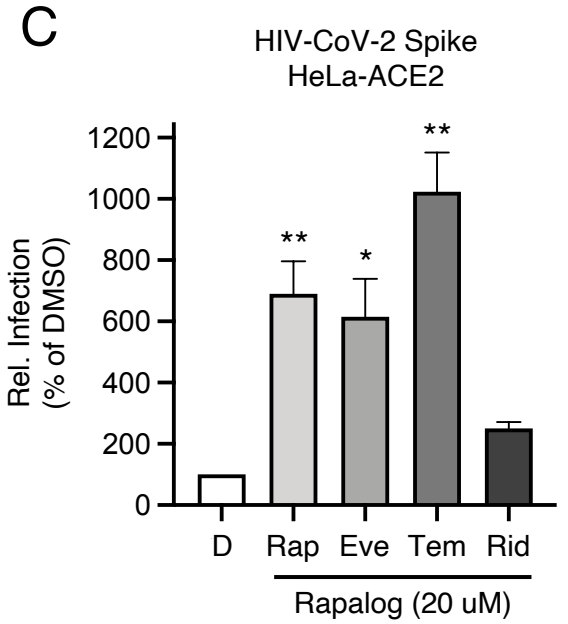
C
HIV-CoV-2 Spike
HeLa-ACE2
Rel. Infection
(% of DMSO)
1200
1000
800
600
400
200
0
**
*
**
D
Rap
Eve
Tem
Rid
Rapalog (20 uM)

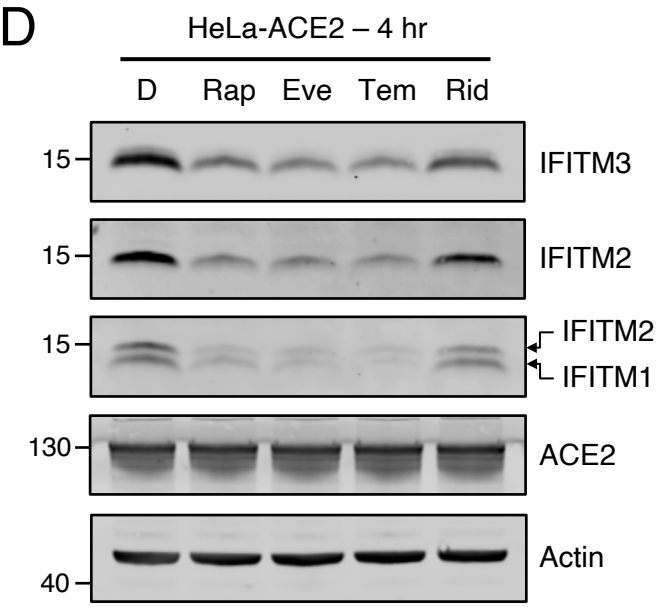
D
HeLa-ACE2 – 4 hr
D
Rap
Eve
Tem
Rid
15
IFITM3
15
IFITM2
15
IFITM2
IFITM1
130
ACE2
40
Actin

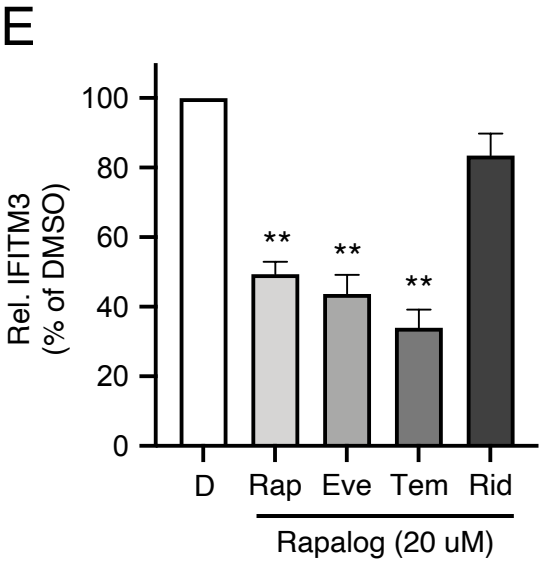
E
Rel. IFITM3
(% of DMSO)
100
80
60
40
20
0
**
**
**
D
Rap
Eve
Tem
Rid
Rapalog (20 uM)

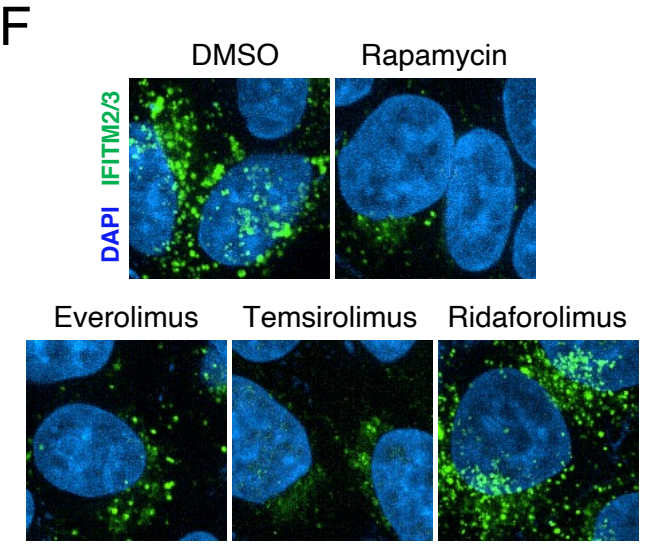
F
DMSO
Rapamycin
DAPI
IFITM2/3
Everolimus
Temsirolimus
Ridaforolimus

Figure 4

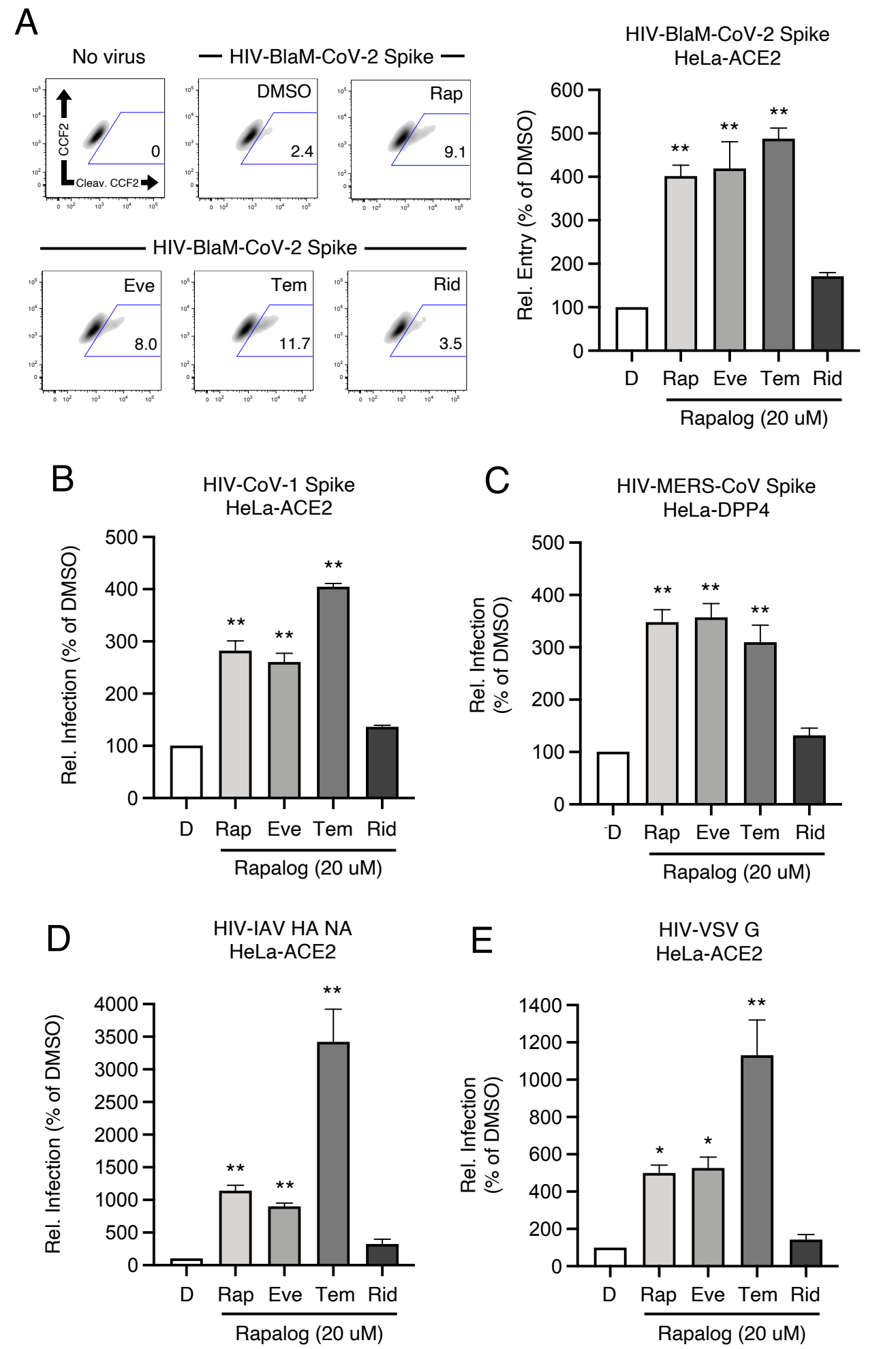
A
No virus
HIV-BlaM-CoV-2 Spike
CCF2
Cleav. CCF2
0
DMSO
2.4
Rap
9.1
HIV-BlaM-CoV-2 Spike
Eve
8.0
Tem
11.7
Rid
3.5
HIV-BlaM-CoV-2 Spike
HeLa-ACE2
Rel. Entry (% of DMSO)
D
Rap
Eve
Tem
Rid
Rapalog (20 uM)
B
HIV-CoV-1 Spike
HeLa-ACE2
Rel. Infection (% of DMSO)
C
HIV-MERS-CoV Spike
HeLa-DPP4
D
HIV-IAV HA NA
HeLa-ACE2
E
HIV-VSV G
HeLa-ACE2

Figure 5

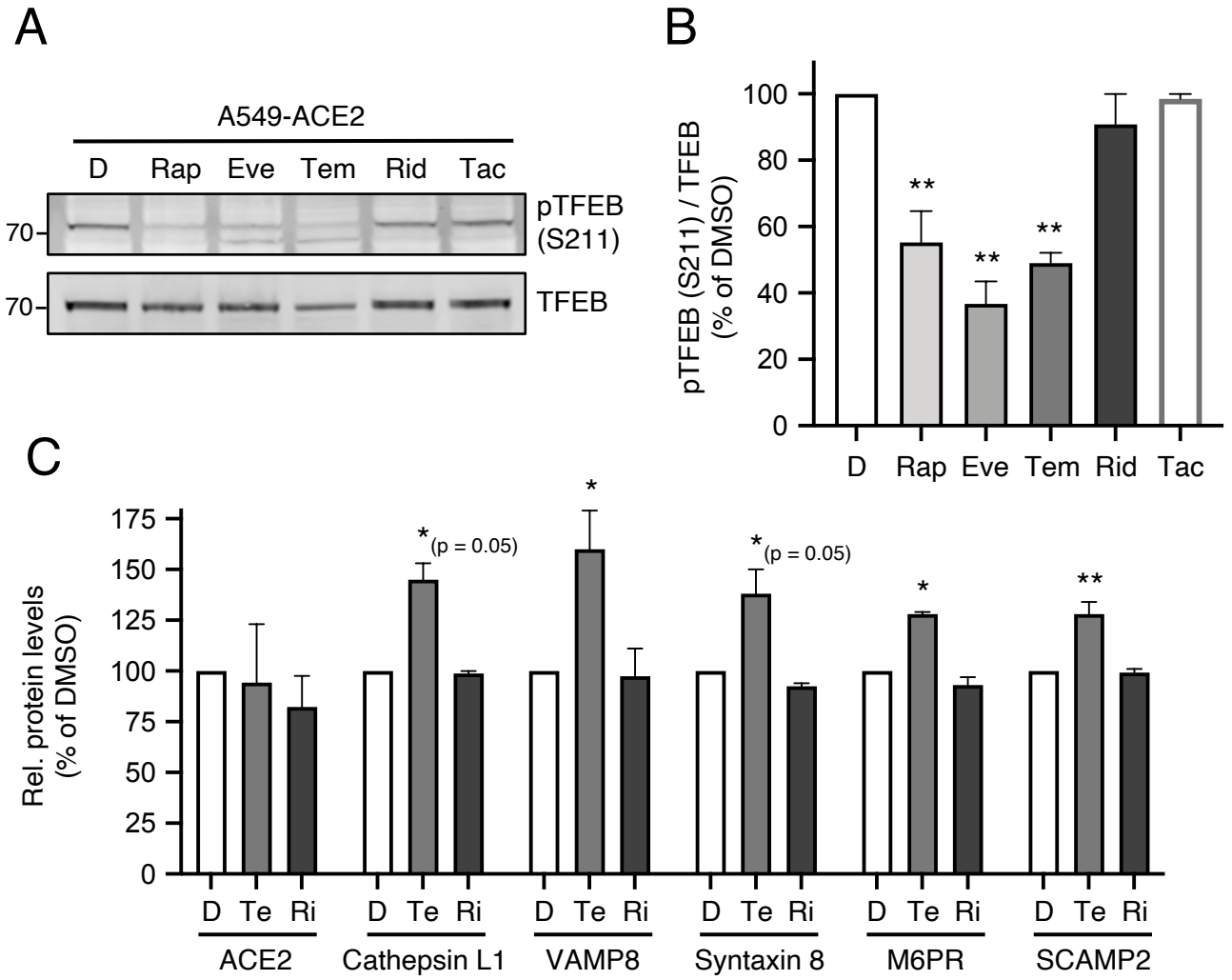
A
A549-ACE2
D
Rap
Eve
Tem
Rid
Tac
70
70
pTFEB
(S211)
TFEB
B
pTFEB (S211) / TFEB
(% of DMSO)
100
80
60
40
20
0
**
**
**
D
Rap
Eve
Tem
Rid
Tac
C
Rel. protein levels
(% of DMSO)
175
150
125
100
75
50
25
0
*(p = 0.05)
*
*(p = 0.05)
*
**
D
Te
Ri
ACE2
Cathepsin L1
VAMP8
Syntaxin 8
M6PR
SCAMP2

Figure 6

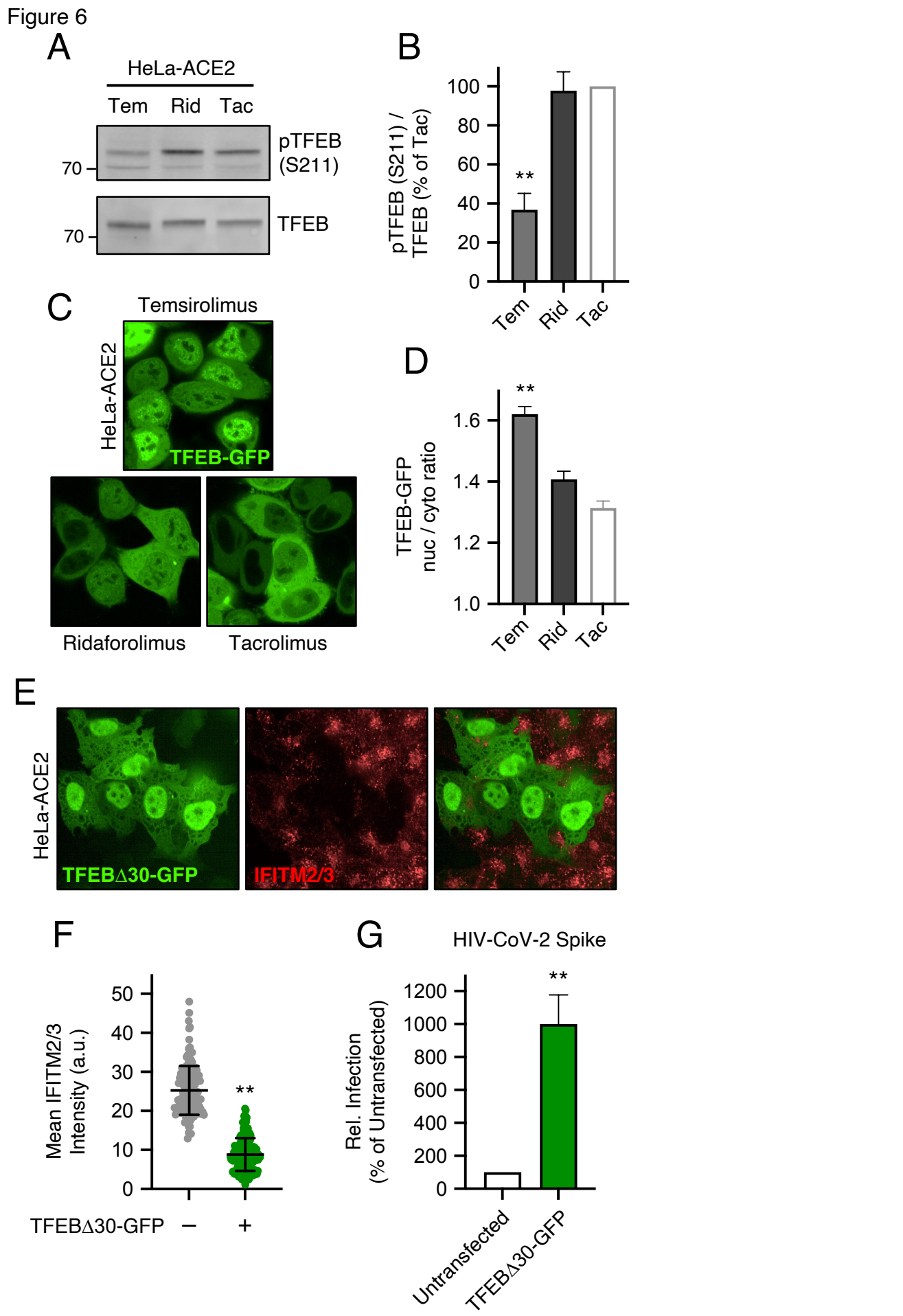
A
HeLa-ACE2
Tem
Rid
Tac
70
pTFEB (S211)
70
TFEB
B
pTFEB (S211) / TFEB (% of Tac)
100
80
60
40
20
0
**
Tem
Rid
Tac
C
Temsirolimus
HeLa-ACE2
TFEB-GFP
Ridaforolimus
Tacrolimus
D
TFEB-GFP nuc / cyto ratio
1.6
1.4
1.2
1.0
**
Tem
Rid
Tac
E
HeLa-ACE2
TFEBΔ30-GFP
IFITM2/3
F
Mean IFITM2/3 Intensity (a.u.)
50
40
30
20
10
0
**
TFEBΔ30-GFP
–
+
G
HIV-CoV-2 Spike
Rel. Infection (% of Untransfected)
1200
1000
800
600
400
200
0
**
Untransfected
TFEBΔ30-GFP

Figure 7

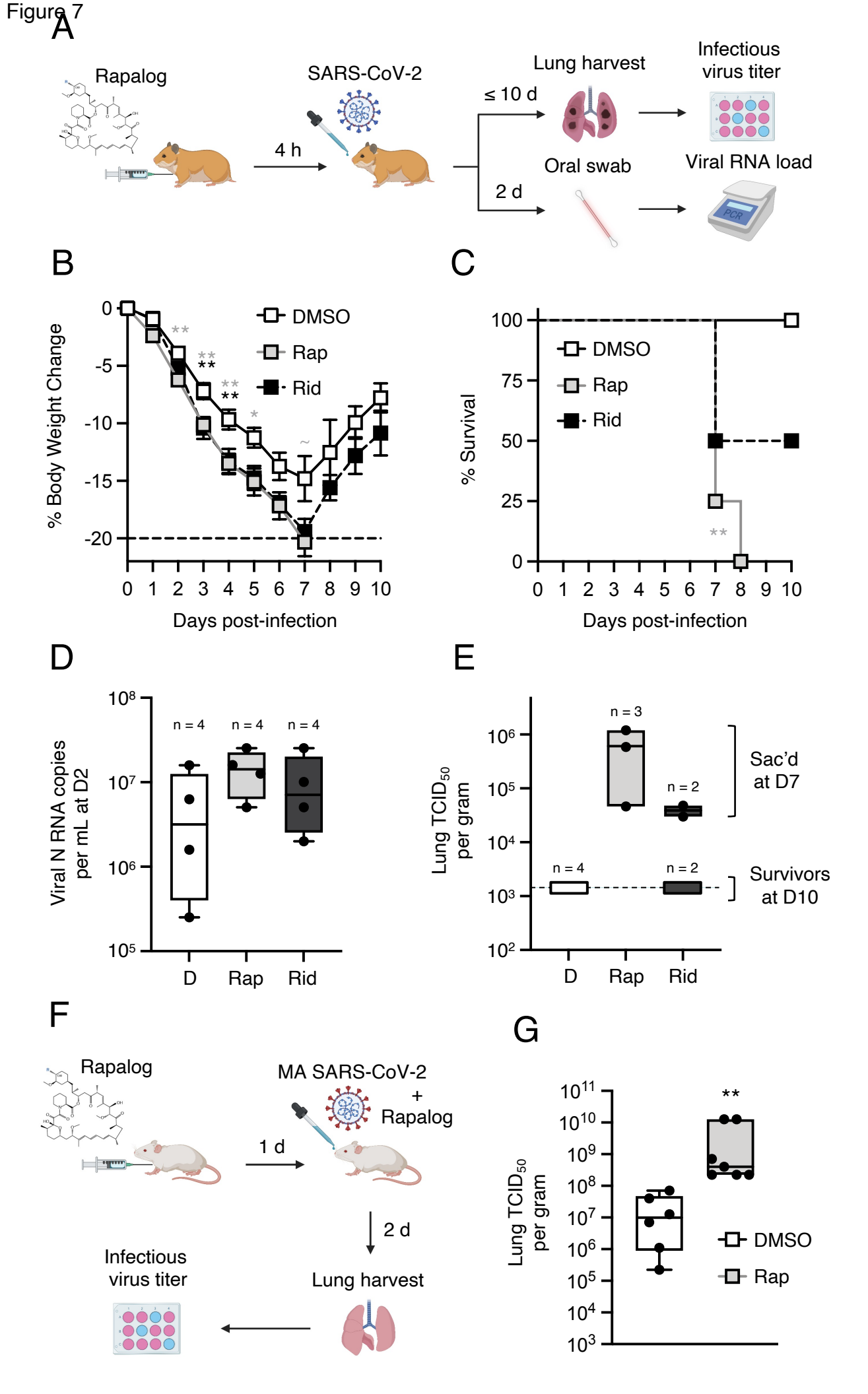
A
Rapalog
SARS-CoV-2
4 h
≤ 10 d
Lung harvest
Infectious virus titer
2 d
Oral swab
Viral RNA load
PCR
B
% Body Weight Change
Days post-infection
DMSO
Rap
Rid
C
% Survival
Days post-infection
DMSO
Rap
Rid
D
Viral N RNA copies per mL at D2
n = 4
n = 4
n = 4
D
Rap
Rid
E
Lung TCID50 per gram
n = 3
n = 2
n = 4
n = 2
Sac'd at D7
Survivors at D10
D
Rap
Rid
F
Rapalog
MA SARS-CoV-2
+
Rapalog
1 d
2 d
Lung harvest
Infectious virus titer
G
Lung TCID50 per gram
DMSO
Rap

Figure 8

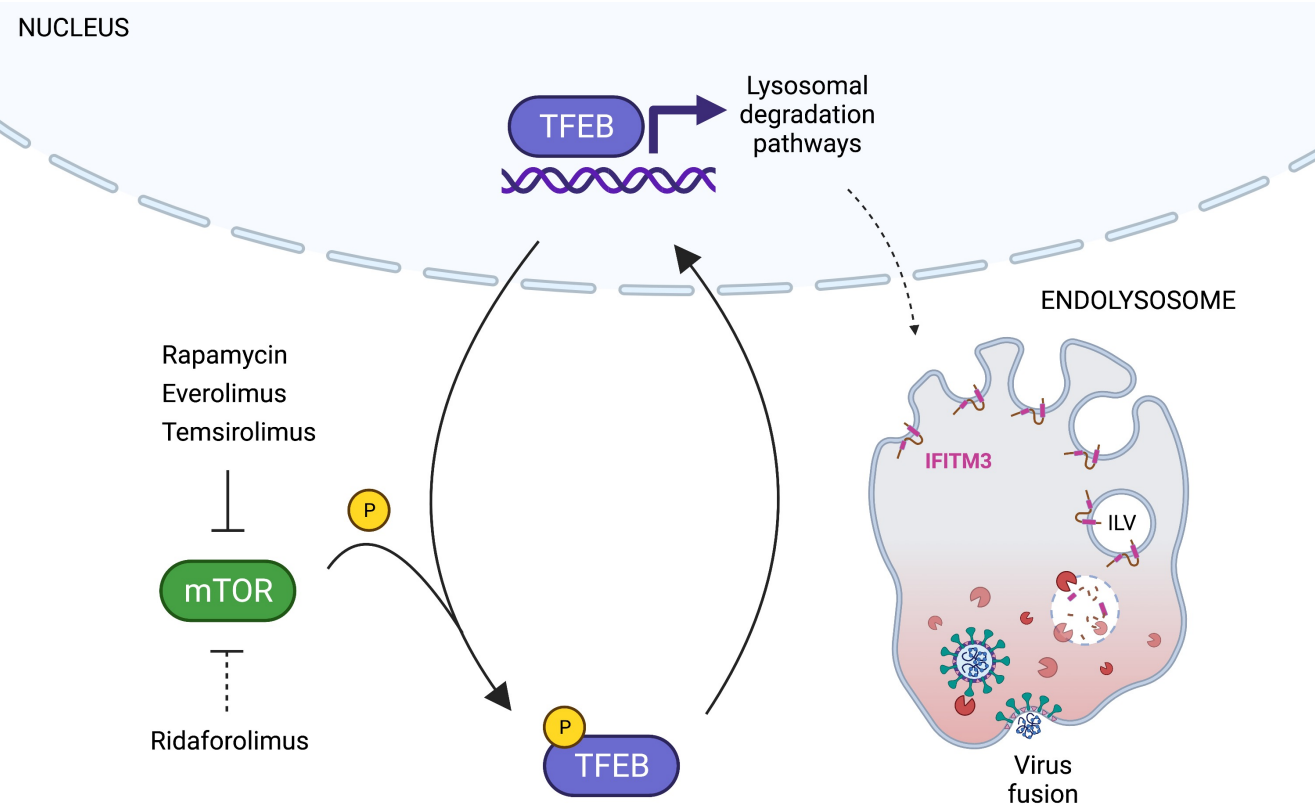
NUCLEUS
TFEB
Lysosomal degradation pathways
ENDOLYSOSOME
Rapamycin
Everolimus
Temsirolimus
mTOR
Ridaforolimus
P
P
TFEB
IFITM3
ILV
Virus fusion

Supplemental Figure 1

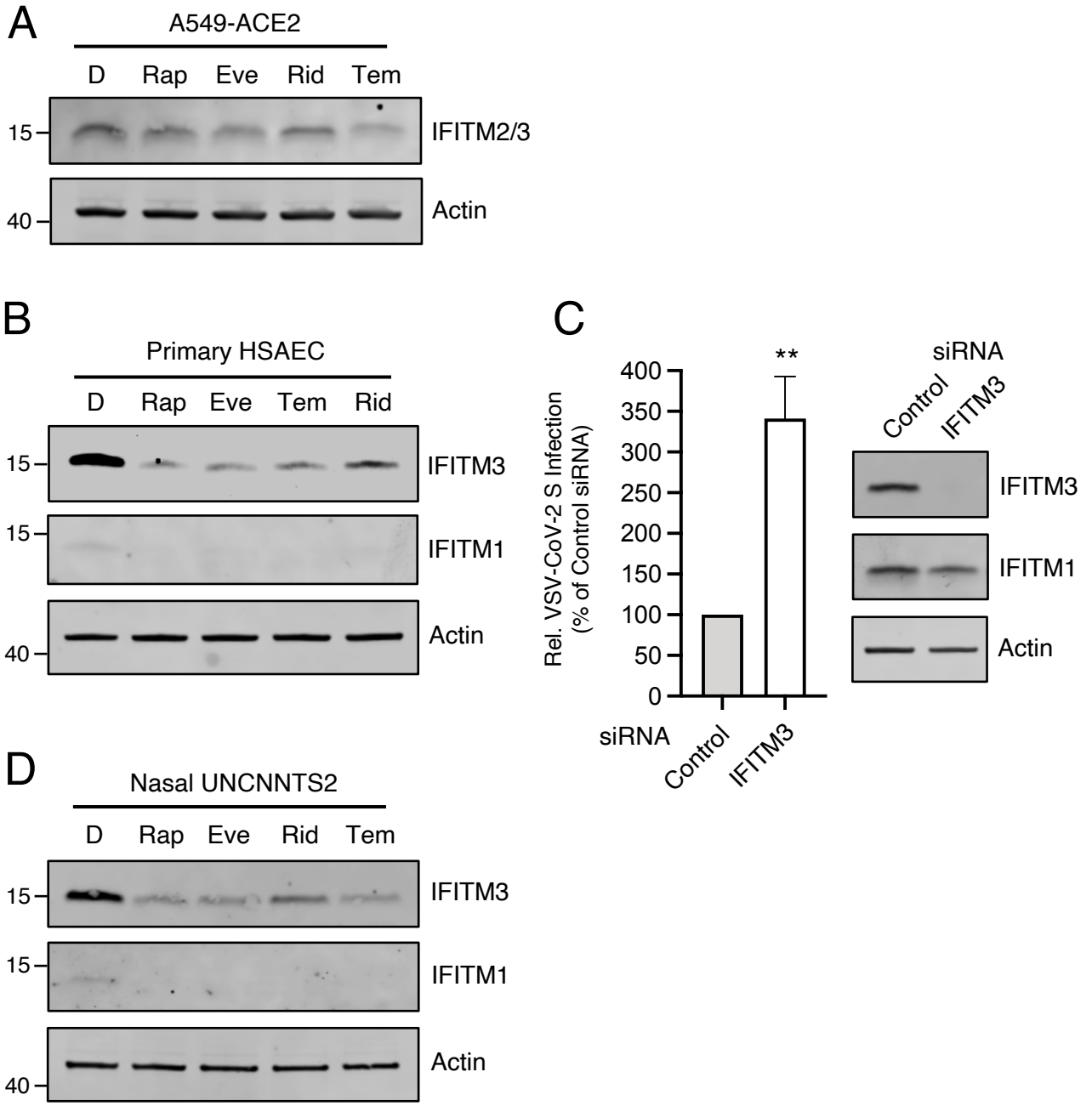

Supplemental Figure 2

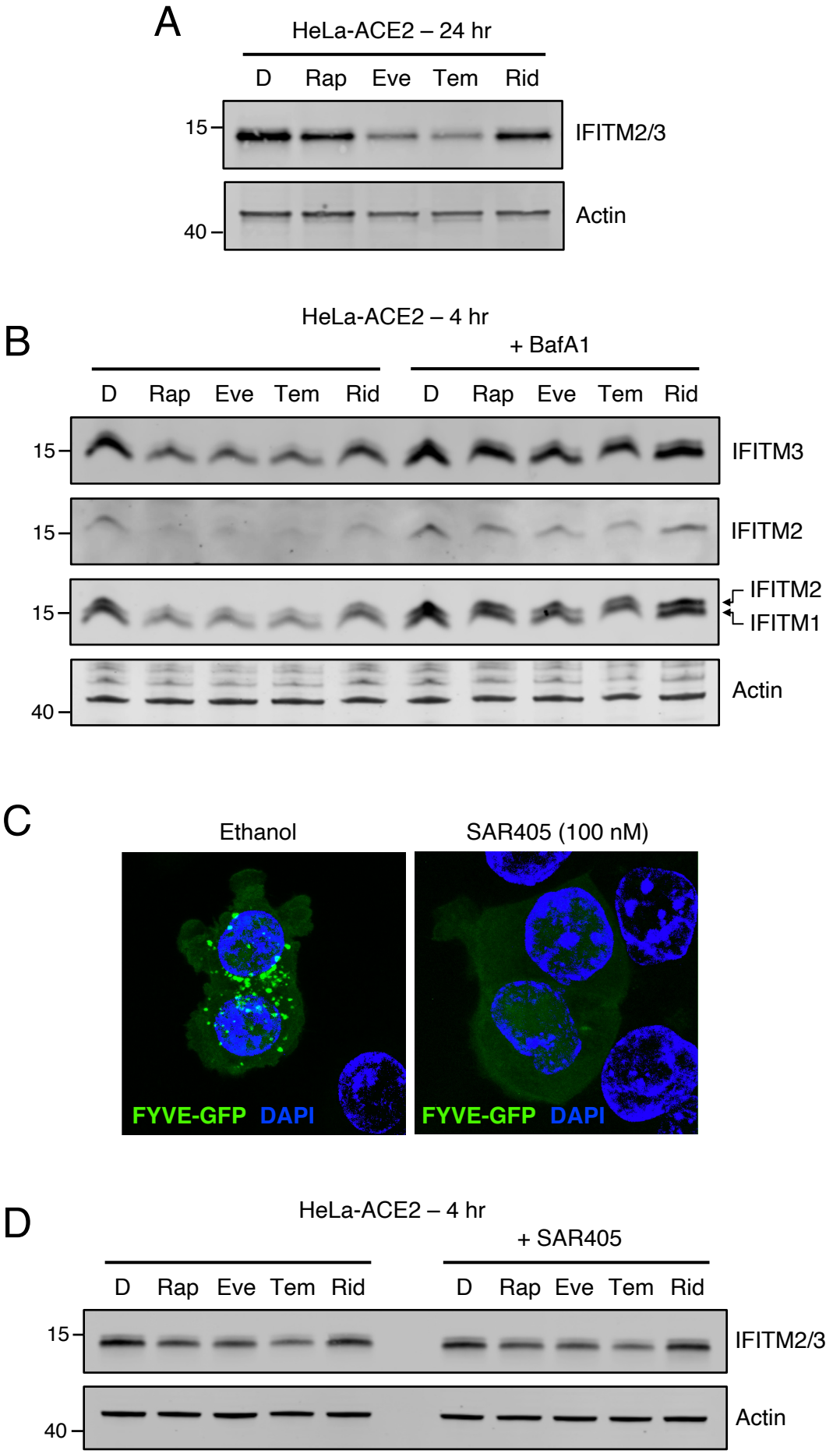

Supplemental Figure 3

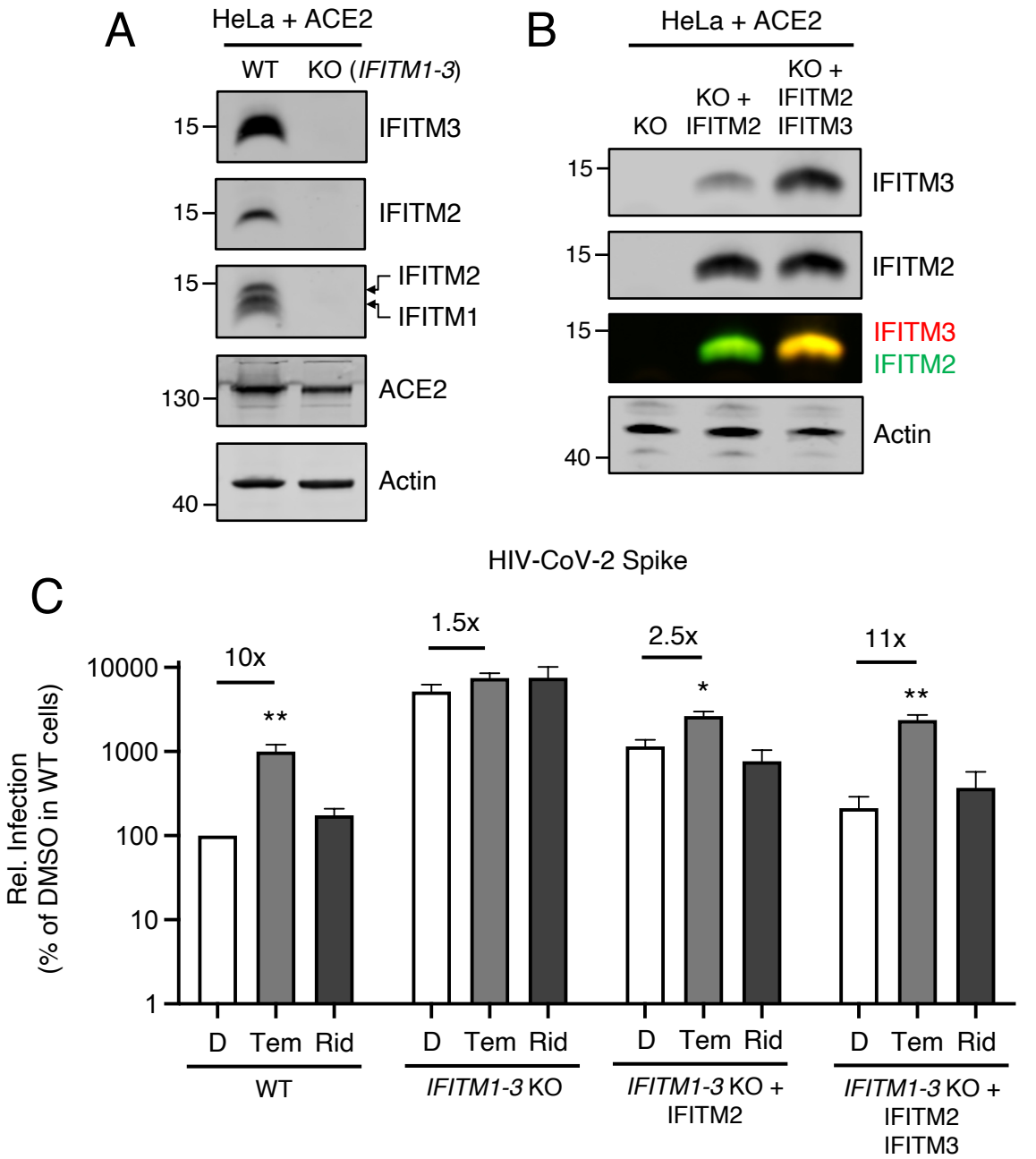
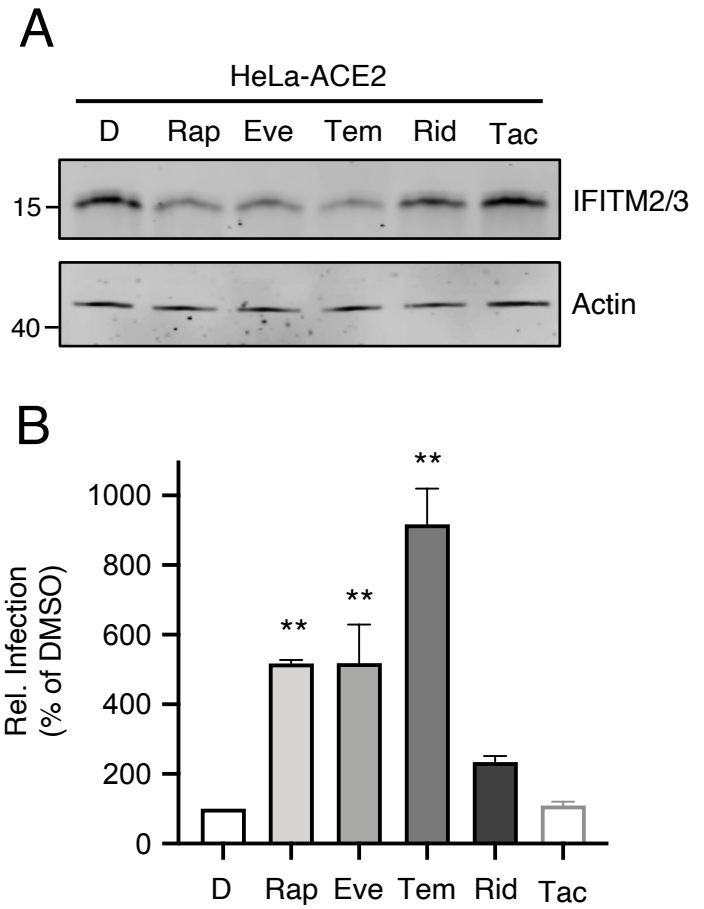
Supplemental Figure 4